

Variational Modeling of Ionic Polymer-Based Structures

by

Miles A Buechler

Thesis submitted to the Faculty of the
Virginia Polytechnic Institute and State University
in partial fulfillment of the requirements for the degree of

Master of Science

in

Mechanical Engineering

Donald J. Leo, Chair
Daniel J. Inman
Harry Robertshaw

July 2005
Blacksburg, Virginia

Keywords: Variational Modeling, Hamilton's Principal, Ionic Polymers

Copyright by Miles A Buechler, 2005

Variational Modeling of Ionic Polymer-Based Structures

Miles A Buechler, M.S.

Virginia Polytechnic Institute and State University, 2005

Advisor: Donald J. Leo

ABSTRACT

Ionomeric polymers are a promising class of intelligent material which exhibit electromechanical coupling similar to that of piezoelectric bimorphs. Ionomeric polymers are much more compliant than piezoelectric ceramics or polymers and have been shown to produce actuation strain on the order of 2% at operating voltages between 1 V and 3 V (Akle et al., 2004). Their high compliance is advantageous in low force sensing configurations because ionic polymers have a very little impact on the dynamics of the measured system. Here we present a variational approach to the dynamic modeling of structures which incorporate ionic polymer materials. The modeling approach requires a priori knowledge of three empirically determined material properties: elastic modulus, dielectric permittivity, and effective strain coefficient. Previous work by Newbury and Leo has demonstrated that these three parameters are strongly frequency dependent in the range between less than 1 Hz to frequencies greater than 1 kHz. Combining the frequency-dependent material parameters with the variational method produces a second-order matrix representation of the structure. The frequency dependence of the material parameters is incorporated using a complex-property approach similar to the techniques for modeling viscoelastic materials. Three structural models are developed to demonstrate this method. First a cantilever beam model is developed and the material properties of a typical polymer are experimentally determined. These properties are then used to simulate both actuation and sensing response of the transducer. The simulations compare very well to the experimental results. This validates the variational method for modeling ionic polymer structures. Next, a plate model is developed in cylindrical coordinates and simulations are performed using a variety of boundary conditions. Finally a plate model is developed in cartesian coordinates. Methods

for applying non-homogenous boundary conditions are then developed and applied to the cartesian coordinate model. Simulations are then compared with experimental data. Again the simulations closely match the experiments validating the modeling method for plate models in 2 dimensions.

Acknowledgments

I would like to express my appreciation to the following individuals and institutions for their support, advice, and understanding.

- Dr. Donald Leo for allowing me to work on this project and more importantly for allowing me to make my own mistakes along the way.
- Matthew Bennett and Barbar Akle for manufacturing the materials used throughout this research as well as helping me to hammer out ideas.
- Curt Kothera and Kevin Farinholt for giving me advice which has been valuable throughout this research.
- Triton Systems Incorporated, Boston, MA for funding this research through an AFOSR-supported Phase II STTR.

Contents

Abstract	ii
Acknowledgments	iv
List of Tables	vii
List of Figures	viii
Chapter 1 Introduction	1
1.1 Ionomeric Material Characteristics	1
1.2 Review of Recent Modeling Methods	3
1.2.1 Physical models of Ionomeric Materials	3
1.2.2 Empirical and Semi-Empirical Models of Ionomeric Materials	4
1.3 Motivation	8
1.4 Research Goals and Contributions	8
1.5 Overview	9
Chapter 2 Modeling Methodology	10
2.1 Hamilton's Principal	11
2.2 Assumed Shape Functions	12
2.3 Variational Principal	13
2.4 Chapter Summary	15
Chapter 3 Cantilever Beam Example and Material Characterization	16
3.1 Assumptions and Simplifications	16
3.2 Actuator and Sensor Equations	18

3.3	Material Characterization	18
3.3.1	Experimental Setup	19
3.3.2	Material Parameter Estimation	22
3.3.3	Identified Material Properties	26
3.4	Model Validation	26
3.5	Chapter Summary	29
Chapter 4 Plate Modeling and Experimental Validation		31
4.1	Plate Model in Cylindrical Coordinates	31
4.1.1	Simulations of Ionic Polymer Disks	33
4.2	Cartesian Coordinates	36
4.2.1	Expanded Potential Energy Function	36
4.2.2	Assumptions and Development	37
4.2.3	Experimental Setup	39
4.2.4	Experimental Results and Model Validation	42
4.3	Chapter Summary	49
Chapter 5 Conclusions		50
5.1	Accomplishments and Contributions	50
5.2	Recommendations for further improvement of this work	52
Bibliography		55
Vita		57

List of Tables

1.1	Comparison of Properties for Several Active Materials	2
3.1	Comparison of Resonance and Damping Parameters	23
3.2	Resonance Parameters for Free Deflection	28
4.1	Weighted Natural Frequencies for Circular Plate	33

List of Figures

1.1	Equivalent Electrical Circuit	5
1.2	Tadokoro's Electrical Impedance Model	7
2.1	Modeling Method Flow Chart	10
3.1	Transducer geometry	17
3.2	Modulus and electrical impedance test setup	20
3.3	Free deflection test setup	21
3.4	Displacement sensing test setup	21
3.5	Mechanical stiffness measurements and curve fit	22
3.6	Electrical impedance measurements	24
3.7	Free deflection at the actuator tip	25
3.8	Complex Material Parameters 0.1Hz - 500Hz	26
3.9	Free Deflection at three points along the actuator	27
3.10	Comparison of deflection shape to structural mode-shapes	29
3.11	Comparison experimental sensing response to the model	30
4.1	Geometry of Plate in Cylindrical Coordinates	32
4.2	Effects of boundary conditions on center point deflection	34
4.3	Effects of boundary conditions resonant deflection shapes	35
4.4	Comparison of 2 nd resonant shapes	36
4.5	Square plate geometry used used in simulations	37
4.6	Experimental specimen geometry	39
4.7	Experimental test fixture	40
4.8	Experimental test setup	41

4.9	Measurement points	42
4.10	Effect of model updating at the center point	43
4.11	Comparison of experiment and simulation at the center point	44
4.12	Comparison of experiment and simulation at (x=4mm,y=4mm)	45
4.13	Comparison of experiment and simulation at (x=16mm,y=12mm)	46
4.14	Comparison of simulated and experimental deflection at 70 Hz	47
4.15	Comparison of simulated and experimental deflection at 108 Hz	48
4.16	Comparison of simulated and experimental deflection at 180 Hz	48
4.17	Comparison of simulated and experimental deflection at 265 Hz	49

Chapter 1

Introduction

Ionomeric polymers are a promising class of intelligent material which exhibit electromechanical coupling similar to that of piezoelectric bimorphs. Ionomeric polymers are much more compliant than piezoelectric ceramics or polymers and have been shown to produce very high actuation strain at low excitation voltages. Their high compliance potentially makes them very good sensors for structural applications. Much of the ongoing ionic polymer research focuses on improvement of the materials and manufacturing methods. One of the recent advancements has been the production of materials which do not require hydration. These transducers are stable in room temperature atmospheric conditions. To assist in developing applications for ionomeric materials this work focuses on the modeling of structures which contain ionomeric transducers.

1.1 Ionomeric Material Characteristics

Ionomeric polymer transducers, also called ionic polymer metal composites (IPMC), consist of an ion-selective membrane sandwiched between two conductive metal electrodes. The ion-selective membrane is infused with mobile cations (positively charged ions). These cations move towards the cathode (negatively charged electrode) upon application of an electric field (Nemat-Nasser and Thomas, 2001). The migration of cations causes a swelling of the material near the cathode and a contraction of the material near the anode resulting in a bending response towards the anode. The inverse operation also takes place. When an IPMC is mechanically deformed in bending the positive and negative strain at opposing sides of the neutral axis cause a charge imbalance and the mobile cations migrate to achieve

electrostatic equilibrium. This phenomena can be applied to sensor technology. Ionomeric materials exhibit several characteristics which are potentially advantageous for both actuator and sensor development. Table 1.1 compares ionic polymer materials to two potential competitors. Ionic polymers are highly compliant as compared to either PVDF or PZT. This is an advantage in sensor configurations because the sensors would have less impact on the system. They also achieve extremely high actuation strain at very small electric fields. This suggests that they could be used as large displacement, low voltage actuators.

Table 1.1: Comparison of Properties for Several Active Materials

Material	Modulus	Strain	Excitation (V)
Ionic Polymer	200 MPa	> 5%	1-3V
PVDF	1GPa	0.1%	100 V
PZT	70GPa	0.1%	100-1000V

The majority of research concerning IPMC's has been performed using hydrated materials. Hydrated materials are those which use water as the solvent. A few years ago, according to Tadokoro and Oguro, two of the most important advancements that needed to be made in order for IPMC's to become viable sensors and actuators were the stabilization of the materials and development of modeling methods (Tadokoro et al., 2001). The development of a system level modeling method is the subject of this research project, but applications for these materials are only now becoming viable because of recent work which has addressed the stabilization of the material.

The solvent (water) is the limiting factor in the environmental stability and longevity of these hydrated samples. Water evaporates under normal atmospheric conditions and also disassociates into hydrogen and oxygen when the applied electric field reaches the electrolysis limit of about 1.2 V. Bennett and Leo also showed the actuation limit of a typical hydrated transducer to be about 1000 cycles. They have greatly improved the stability of IPMC's by replacing water with ionic liquids, which are salts that remain liquid at room temperature. In a study which used 1-ethyl-3-methylimidazolium trifluoromethanesulfonate (EMI-Tf) the actuation limit of a transducer was extended to nearly 250,000 cycles (Bennett and Leo, 2004). The primary drawback of ionic liquid materials as compared to early hydrated materials is speed. Ionic liquid materials have been shown to be slower than their water

hydrated counterparts.

1.2 Review of Recent Modeling Methods

1.2.1 Physical models of Ionomeric Materials

A relatively recent model of ionomeric materials suggested that fluid transport was the primary mechanism responsible for the bending response exhibited by ionic polymer devices (Tadokoro et al., 2000). According to the authors, when electric potential is applied across the polymer thickness mobile cations move towards the cathode or negative electrode. As the cations move across the thickness they carry with them water (water was the solvent in the materials studied) molecules. They believed that the depletion of water near the anode caused a contraction of the material and likewise the material swelled near the cathode. This was the mechanism of actuation in their model.

Another model proposed at about the same time suggested that electrostatic forces, rather than hydraulic pressures were responsible for the bending and sensing response (Nemat-Nasser and Li, 2000). The basic idea was that application of an electric field caused the mobile cations to move to the cathode. The abundance of cations results in an expansion at the cathode, and a contraction at the anode. It is this expansion and contraction at opposing sides of the device's neutral plane which causes the transducer to bend toward the anode. Also, under an applied load the mechanical contraction and expansion at opposing sides of the neutral plane causes ion migration resulting in net charge at the electrodes. Their model resulted in a set of coupled linearized differential equations based on physical properties of the polymer chain, solvent, and counter ion. They manufactured a hydrated sample and performed both sensing and actuation experiments, which were compared to simulations. Their comparisons were fairly good. As an example they applied a sinusoidal voltage and the resulting time domain response compared favorably to the model predictions. They matched the amplitude of the response very well; however, there was a phase shift of about 45 degrees between the model and experiment. They also compared sensing response to a step displacement applied at the actuator tip for several actuator lengths. Their experimental results exhibit quite a bit of scatter but the average of the data does appear to follow the predicted curve.

1.2.2 Empirical and Semi-Empirical Models of Ionomeric Materials

Many of the first models of ionic polymer materials were empirical models. One of these models proposed that tip response to an applied step voltage could be modeled as a sum of exponentials (Kanno et al., 1994). They performed experiments and performed a least squares curve fit to the time domain results. This was performed with many different input levels. The result of this analysis was that the coefficients of the exponential did not vary linearly with input voltage.

Another empirical model developed by Newbury and Leo was useful for predicting both actuating and sensing response (Newbury and Leo, 2002).

$$\begin{Bmatrix} v(\omega) \\ f(\omega) \end{Bmatrix} = \begin{bmatrix} Z_{11} & Z_{12} \\ Z_{21} & Z_{22} \end{bmatrix} \begin{Bmatrix} i(\omega) \\ \dot{u}(\omega) \end{Bmatrix}, \quad (1.1)$$

where the applied voltage v , applied force f , resulting current i , and tip velocity \dot{u} are all functions of frequency ω . The parameter Z_{11} is the electrical impedance with \dot{u} set to zero, Z_{22} is the mechanical impedance with the current set to zero (open circuit), and Z_{12} and Z_{21} are parameters associated with the electromechanical coupling. Several experiments were then performed to determine these parameters. A step velocity was applied at the tip while measuring force and short circuit voltage which were used to show a relationship between Z_{11} and Z_{12} . Then the electrical impedance was measured with a blocked tip to determine Z_{11} . A force was then applied under open circuit electrical boundary conditions to determine Z_{22} . Finally, Z_{21} was determined from an experiment using a step current input and blocked boundary conditions. A numerical optimization algorithm was employed to fit Zero, pole, gain models to the parameters. Next they validated the models with a series of experiments that were not used in the curve fitting. They achieved very good results that validated the model. However, the model did not include the geometry of the transducer in the analysis and therefore could not be used to simulate a transducer of a different geometry.

To remedy the scalability issue of their first model Newbury and Leo developed a model which incorporated transducer geometry and some widely accepted physical phenomena (Newbury and Leo, 2003a). It begins with an equivalent circuit of the form shown in Figure 1.1. The left side of the circuit represents the electrical impedance of the transducer while the right side of the model represents the mechanical impedance. The electromechani-

cal coupling is represented by the transformer in the middle. The components Z_p , Z_{m1} , and Z_{m2} were considered to be dependent on both intrinsic material properties and transducer geometry.

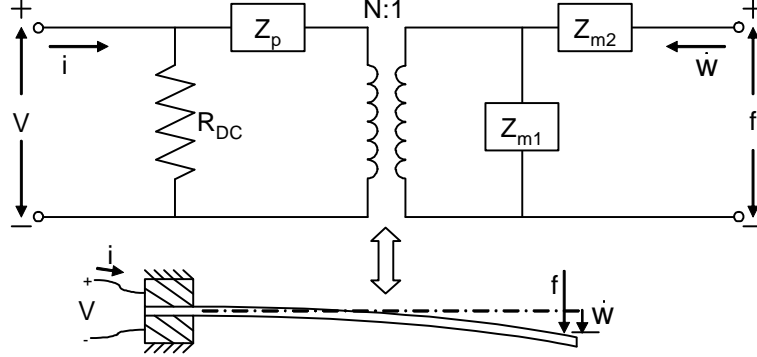


Figure 1.1: Equivalent Electrical Circuit

Some initial experiments showed that the material was weakly coupled resulting in an electrical impedance that is not dependent on mechanical boundary conditions and a mechanical impedance which is not dependent on electrical boundary conditions. This simplified the analysis and resulted in a set of linear equations which were very similar to Equation 1.1. This set of linear equations is

$$\begin{Bmatrix} v(\omega) \\ f(\omega) \end{Bmatrix} = \begin{bmatrix} \frac{Z_p}{1+Z_p/R_{dc}} & N \frac{Z_{m1}}{1+Z_p/R_{dc}} \\ N \frac{Z_{m1}}{1+Z_p/R_{dc}} & Z_{m1} + Z_{m2} \end{bmatrix} \begin{Bmatrix} i(\omega) \\ \dot{u}(\omega) \end{Bmatrix}. \quad (1.2)$$

Frequency domain models of the parameters Z_p , Z_{m1} , and Z_{m2} were then fit to experimental data while considering their geometry dependence. This resulted in a model which could be used to predict the response of transducers of different geometry.

An additional contribution of this model which greatly influenced this research project was the direct determination of quasi-piezoelectric properties from these experimental results. In order to more easily compare ionic polymer materials to other electro mechanically coupled materials the authors determined the equivalent frequency dependent modulus, dielectric permittivity, and strain coefficients which would result in the actuation and sensing response modeled by Equation 1.2.

The model developed by Newbury and Leo was expanded by Franklin to include the effect of passive layers added to the ionomeric cantilever beam (Franklin, 2003). This model development essentially involved computing a composite stiffness which accounted for both the relative thickness of the layers as well as the different material properties. The greatest

contribution of Franklins work to this thesis is an improved method for determining the viscoelastic parameters of the modulus. In Newbury's method a cantilever beam configuration was used and the load cell was moved a measurable distance. In the low frequency range studied by Newbury this was adequate; however, Franklin found that at higher frequencies the load cell began acting like an accelerometer and only measuring its own accelerations instead of the load applied to the specimen. To remove the accelerometer affect a sliding pinned test configuration was employed. In this way the clamped end of beam was moved a known distance while a stationary load cell measured the force at the tip. The mechanical stiffness in this configuration was found to be

$$K(s) = \frac{1}{\sum_{k=1}^n \frac{1}{M_k s^2 + K_k}} \left\{ Y(s) I \sum_{k=1}^n \frac{\Phi_{k,xxx}}{M_k s^2 + K_k} \right\}, \quad (1.3)$$

where $\Phi_{k,xxx}$ is the third spatial derivative of the sliding-pinned mode shape, $M_k = \rho b h L_f$, and $K_k(s) = Y(s) I L_f \beta_k^4$. β_k is the weighted natural frequency corresponding to a sliding-pinned beam (Blevins, 1995). This is a much improved method of measuring the mechanical stiffness and was employed in this research.

In addition to the physical model Tadokoro also developed a semi-empirical model which included three stages (Tadokoro et al., 2001). The first of these steps was an electrical stage. The input to this stage is voltage and the output of the stage is current so it is essentially electrical impedance. Where it differs from other methods of modeling the electrical impedance is that the input voltage and subsequent current are not constants throughout the beam. The transducer is broken up into several elements and the resistivity of the electrode as well as the base polymer are considered. In Figure 1.2 several elements of this model are shown. The electrode is considered entirely resistive while the polymer is modeled with resistors and capacitors resulting in frequency dependence.

The next stage dubbed the stress generation stage is very similar to many other models of electro mechanically coupled materials. In this stage stress is related to mechanical strain and current through the equation

$$\sigma = D(s)\epsilon - e \frac{\omega_n^2 s}{s^2 + 2\zeta\omega_n s + \omega_n^2} i \quad (1.4)$$

where D is the stiffness matrix, e is the stress generation matrix and the terms ω_n and ζ are parameters giving frequency dependence to the coupling. The final stage is the mechanical stage where mass and stiffness matrices are developed along with a proportional damping

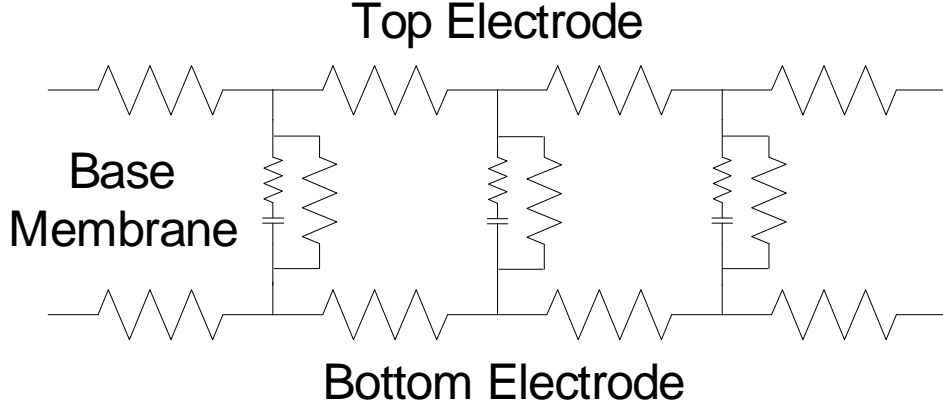


Figure 1.2: Tadokoro's Electrical Impedance Model

matrix. The disadvantage of this method is that solving for each part separately rather than coupling the equation does not allow the system to be used to model both sensing and actuation. This model is very good for predicting actuator behavior but is incapable of making sensor predictions.

Other Active Material Models

The previous models were all developed specifically with ionomeric materials in mind; however, we can learn quite a bit from methods used to model other electro mechanically coupled materials. One such method which was extremely influential in this work was developed by Hagood to model piezoelectric actuator structure interaction (Chang and Hagood, 1994). Hagood began with a constitutive equation of the form

$$\begin{Bmatrix} \underline{D}' \\ \underline{T}' \end{Bmatrix} = \begin{bmatrix} \epsilon^{\underline{S}} & \underline{e} \\ -\underline{e} & \underline{c}^{\underline{E}} \end{bmatrix} \begin{Bmatrix} \underline{E}' \\ \underline{S}' \end{Bmatrix}, \quad (1.5)$$

where \underline{D} is the electric displacement vector, \underline{T} is the stress vector, \underline{E} is the electric potential vector, \underline{S} is the strain vector, $\epsilon^{\underline{S}}$ is the permittivity matrix at constant strain, $\underline{c}^{\underline{E}}$ is the stiffness matrix at constant electric potential, and \underline{e} is the coupling matrix. They then defined kinetic and potential energy functions and applied the variational principle resulting in mass, stiffness, and damping matrices which were put into state space and used for control system design. They then performed experiments where they used their control system to actively damp vibrations. Their results were quite good and highlighted the fact that their model was not only good for predicting actuator behavior but also how the actuators interacted with other structures. A more complete explanation of the variational method

and how it is applied to structures containing ionomeric materials is the subject of this research and will be discussed more completely in the remaining chapters.

1.3 Motivation

As mentioned previously one of the steps that must be taken in order to make ionomeric materials a viable alternative in transducer design is to develop design methods. This research was begun in answer to that need. Several applications come to mind that could benefit from a system level modeling method. First of all this research is supported by an interest in developing deformable mirrors based on ionomeric material. Mirrors manufactured from ionic polymers would be much lighter and potentially cheaper to manufacture than traditional glass mirrors. However, the primary advantage of ionic polymers over traditional glass is their ability to deform in a controllable manner. This controlled deformation can be used to change the focal length of the mirror, actively damp vibrations, compensate for lower manufacturing tolerances, and possibly compensate for atmospheric aberrations. The ability of a control system to achieve these desired results will be greatly improved with a good system model which will be developed in this research. In addition to deformable mirrors other applications have been proposed which can benefit from a good modeling method. For instance, optimal sensor placement could be determined by modeling the polymers as part of a greater structure.

1.4 Research Goals and Contributions

The overall goals of this project and how they will contribute to the scientific and engineering community are listed below.

- *Develop a verified model for sensing and actuation.* A unified modeling method will be developed which will allow one set of equations or methods to be used to predict both sensing and actuating responses of a system incorporating some ionic polymer components.
- *Refine methods for determination of material properties.* The modeling method should be scalable. In other words a design engineer should be able to perform experiments with a small less costly ionic polymer system and empirically determine material

properties which can be applied to a larger more complex system. In this work existing material characterization methods have been expanded to and shown to be valid at higher frequencies than previous work.

- *Maintain one modeling methodology for multiple system configurations.* The method developed here is applicable to many system configurations. Developments will be performed in different coordinate systems and boundary conditions, and passive components can be modeled easily.

1.5 Overview

The modeling methods developed in this research consists of a series of steps. Though complete application of the method requires one to define the structure and purpose from which material properties, boundary conditions, shape functions and loading conditions can be derived we will begin the model development in Chapter 2 assuming that we can define shape functions for our structure. Potential and kinetic energy as well as external work functions will be derived conceptually without actually defining the system. We will then apply the variational approach resulting in a set off linear differential equations which can be solved to determine deformation due to an electrical excitation and charge output due to a mechanical excitation.

In Chapter 3 we will apply the method to a cantilever beam. Here we will demonstrate the application of boundary conditions and subsequent shape functions. The model will be completely developed following the steps outlined in Chapter 2. We will then characterize the frequency dependent material properties and validate the modeling method for both actuation and sensing applications.

Chapter four will be dedicated to thin ionic polymer plates which must be modeled in two dimensions. First a plate model will be developed in cylindrical coordinates and some of the interesting results that can be derived from the model will be discussed. Then a plate model will be developed in cartesian coordinates. Experiments will be performed on a square plate manufactured from the same material which is characterized in Chapter 2. These experiments will result in frequency response functions and operational deflection shapes which are then compared with simulations based on the model. These comparisons will show that the model is valid for plate structures.

Chapter 2

Modeling Methodology

In this chapter we will demonstrate the variational principal. The required steps are outlined in Figure 2.1. Here we will assume that material properties, boundary and loading conditions, as well as shape functions have already been defined. We will begin the development with the work and energy functions. The next two chapters will focus on the modeling of specific applications by demonstrating the selection of shape functions based on the boundary conditions as well as the characterization of materials.

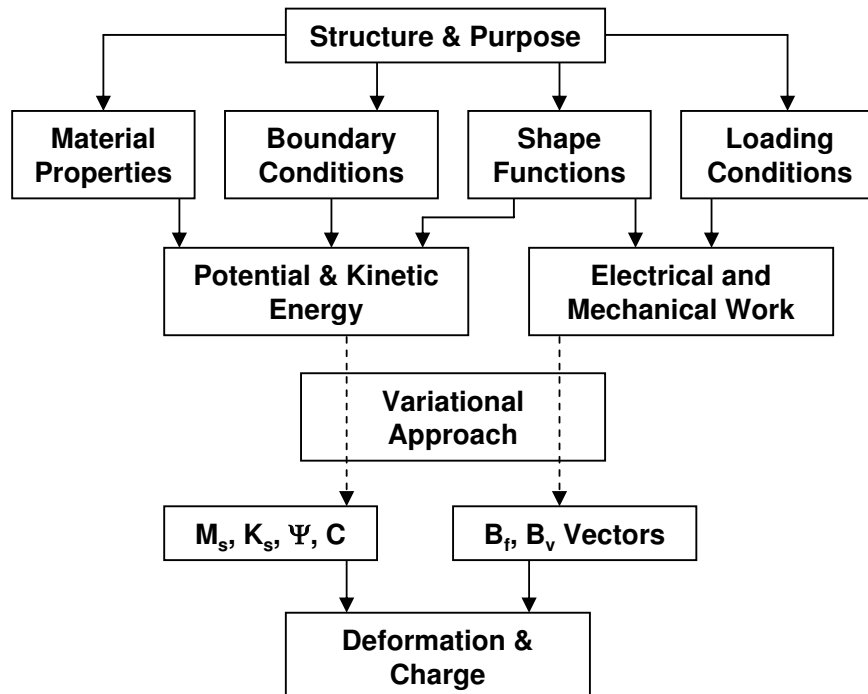


Figure 2.1: Modeling Method Flow Chart

2.1 Hamilton's Principal

We begin with Hamilton's Principle, which states

$$\int_{t_1}^{t_2} \delta\mathcal{T} - \delta\mathcal{V} + \delta\mathcal{W}^{ext} dt = 0 \quad \delta|_{t_1}^{t_2} = 0, \quad (2.1)$$

where $\delta\mathcal{T}$ is the variation in kinetic energy, $\delta\mathcal{V}$ is the variation in potential energy, and $\delta\mathcal{W}^{ext}$ is the variation in external work. The kinetic energy external work are defined by the volume integrals

$$\mathcal{T} = \int_{V_{ol}} \frac{1}{2} \rho \dot{\underline{U}}' \dot{\underline{U}} dV_{ol} \quad \mathcal{W}^{ext} = \int_{V_{ol}} \underline{f} \underline{U} + \underline{V} \underline{q} dV_{ol}, \quad (2.2)$$

where ρ can vary spatially, f can vary spatially and temporally, and in the most general form \underline{U} is a 3 element vector whose elements define the mechanical displacements as functions of space and time. \underline{V} is the electric potential applied on each electrode.

The potential energy (\mathcal{V}) is derived by assuming that the electromechanical coupling mechanism is the same in sensing as in actuation. The symmetry of Equation 1.2 reflects this assumption. For our current purposes we will use the inverse relationship and for convenience we drop the frequency dependence in the notation, but it will be reintroduced later. This results in two constitutive equations,

$$\begin{aligned} \underline{T} &= \mathbf{c}^D \underline{S} - \mathbf{h} \underline{D} \\ \underline{E} &= -\mathbf{h}' \underline{S} + \boldsymbol{\epsilon}^{T^{-1}} \underline{D} \end{aligned} \quad (2.3)$$

where the stress vector (\underline{T}) and strain vector (\underline{S}) consists of 6 elements, and the electric displacement vector (\underline{D}) consists of 3 elements. The components of these vectors are generally function of the spatial variables (x, y, and z in cartesian coordinates) and time, but for simplicity this will not be shown. (\mathbf{c}^D) denotes the 6x6 stiffness matrix with the superscript D indicating it is under constant electric displacement, the electromechanical coupling (\mathbf{h}) is a 6x3 matrix defined as $\mathbf{c}^D \mathbf{d} \boldsymbol{\epsilon}^{T^{-1}}$, the dielectric permittivity ($\boldsymbol{\epsilon}^T$) is a 3x3 symmetric matrix, where the superscript T indicates it was determined under constant stress, and the strain coefficient matrix \mathbf{d} is a 6x3 matrix.

Volumetric potential energy (v) is then related to stress, strain, electric potential, and electric displacement through the differential form of the first law of thermodynamics,

which neglecting thermal work is

$$dv = \underline{T}' d\underline{S} + \underline{E}' d\underline{D}. \quad (2.4)$$

Substituting the first the expression for stress of equation (2.3) into the first law and integrating with respect to strain results in

$$v = \frac{1}{2} \underline{S}' \underline{c}^{\underline{D}} \underline{S} - \underline{D}' \underline{h}' \underline{S} + C_1(\underline{D}), \quad (2.5)$$

Because $\underline{D}' \underline{h}' \underline{S}$ is a scalar we can transpose it for convenience. Then to determine the function $C_1(\underline{D})$ we differentiate with respect to \underline{D}

$$\frac{dv}{d\underline{D}} = -\underline{S}' \underline{h} + \frac{dC_1}{d\underline{D}} = \underline{E}' = -\underline{S}' \underline{h} + \underline{D}' \underline{\epsilon}^{\underline{T}^{-1}} \quad (2.6)$$

or

$$\frac{dC_1}{d\underline{D}} = \underline{D}' \underline{\epsilon}^{\underline{T}^{-1}} \quad (2.7)$$

Finally, we have the volumetric potential energy function

$$v = \frac{1}{2} \underline{S}' \underline{c}^{\underline{D}} \underline{S} - \underline{D}' \underline{h}' \underline{S} + \frac{1}{2} \underline{D}' \underline{\epsilon}^{\underline{T}^{-1}} \underline{D}. \quad (2.8)$$

Integrating over the volume results in the total potential energy function

$$\mathcal{V} = \int_{V_{ol}} \frac{1}{2} \underline{S}' \underline{c}^{\underline{D}} \underline{S} - \underline{S}' \underline{h}' \underline{D} + \frac{1}{2} \underline{D}' \underline{\epsilon}^{\underline{T}^{-1}} \underline{D} dV_{ol}. \quad (2.9)$$

The kinetic energy and work functions of Equation 2.2 are in terms of displacement, but strain (\underline{S}) is related to displacement vector \underline{U} through a differential operator L_u ,

$$\underline{S} = L_u \underline{U}, \quad (2.10)$$

So the potential energy is

$$\mathcal{V} = \int_{V_{ol}} \underbrace{\frac{1}{2} (L_u \underline{U})' \underline{c}^{\underline{D}} L_u \underline{U}}_{\text{Strain Energy}} - \underbrace{(L_u \underline{U})' \underline{h}' \underline{D}}_{\text{Coupling Energy}} + \underbrace{\frac{1}{2} \underline{D}' \underline{\epsilon}^{\underline{T}^{-1}} \underline{D}}_{\text{Dielectric Potential}} dV_{ol}. \quad (2.11)$$

2.2 Assumed Shape Functions

Next we apply separation of variables and write mechanical and electrical displacements as an infinite series

$$\underline{U}(\underline{X}, t) = \sum_{n=1}^{\infty} \Phi_{un}(\underline{X}) A_n(t) \quad \underline{D}(\underline{X}) = \sum_{n=1}^{\infty} \Phi_{Dn}(\underline{X}) q_n(t), \quad (2.12)$$

where Φ_{un} and Φ_{Dn} are the n^{th} mechanical and electrical shape functions respectively. These shape functions must satisfy the kinematic boundary conditions.. If they are orthogonal to each other, computations can be significantly reduced; however orthogonality is not a requirement. These summations are then truncated to a finite sum and written in matrix form

$$\underline{U}(\underline{X}, t) = \underline{\Phi}_u'(\underline{X})\underline{A}(t) \quad \underline{D}(\underline{X}) = \underline{\Phi}_D'(\underline{X})\underline{q}(t). \quad (2.13)$$

Substituting the expression for \underline{U} into the kinetic energy term in Equation 2.2 results in

$$\mathcal{T} = \int_{V_{ol}} \frac{1}{2} \rho \underline{\dot{A}}' \underline{\Phi}_u \underline{\Phi}_u' \underline{\dot{A}} \, dV_{ol}, \quad (2.14)$$

When we substitute the displacements into the potential energy we get

$$\mathcal{V} = \int_{V_{ol}} \frac{1}{2} \underline{A}' (L_u \underline{\Phi}_u')' \mathbf{c}^D L_u \underline{\Phi}_u \underline{A} - \underline{A}' (L_u \underline{\Phi}_u')' \mathbf{h} \underline{\Phi}_D' \underline{q} + \frac{1}{2} \underline{q}' \underline{\Phi}_D \boldsymbol{\epsilon}^T L^{-1} \underline{\Phi}_D' \underline{q} \, dV_{ol}. \quad (2.15)$$

And the external work is

$$\mathcal{W}^{ext} = \int_{V_{ol}} \underline{f} \underline{\Phi}_u' \underline{A} + \underline{V} \underline{q} \, dV_{ol} \quad (2.16)$$

2.3 Variational Principal

The variation in kinetic energy is

$$\delta \mathcal{T} = \int_{V_{ol}} \frac{1}{2} \rho \delta(\underline{\dot{A}})' \underline{\Phi}_u \underline{\Phi}_u' \underline{\dot{A}} + \frac{1}{2} \rho \underline{\dot{A}}' \underline{\Phi}_u \underline{\Phi}_u' \delta(\underline{\dot{A}}) \, dV_{ol}. \quad (2.17)$$

However, $\underline{\dot{A}}' \underline{\Phi}_u \underline{\Phi}_u' \delta(\underline{\dot{A}})$ is a scalar so it can be transposed resulting in

$$\delta \mathcal{T} = \int_{V_{ol}} \rho \delta \underline{\dot{A}}' \underline{\Phi}_u \underline{\Phi}_u' \underline{\dot{A}} \, dV_{ol}. \quad (2.18)$$

After integrating by parts from t_1 to t_2 , and applying the previously stated condition that the variations are zero at t_1 and t_2 , we have

$$\delta \mathcal{T} = \delta \underline{A}' \left[\int_{V_{ol}} -\rho \underline{\Phi}_u' \underline{\Phi}_u \, dV_{ol} \right] \underline{\ddot{A}}. \quad (2.19)$$

Applying a similar symmetry relationship we find the variation in strain energy to be

$$\delta \mathcal{V}_{se} = \delta \underline{A}' \left[\int_{V_{ol}} (L_u \underline{\Phi}_u')' \mathbf{c} L_u \underline{\Phi}_u' \, dV_{ol} \right] \underline{A}. \quad (2.20)$$

The variation in coupling potential energy is

$$\delta\mathcal{V}_{couple} = -\delta\underline{A}' \left\{ \int_{V_{ol}} (L_u \underline{\Phi}_u)' \mathbf{h} \underline{\Phi}_D' dV_{ol} \right\} \underline{q} - \delta\underline{q}' \left\{ \int_{V_{ol}} \underline{\Phi}_D \mathbf{h}' (L_u \underline{\Phi}_u)' dV_{ol} \right\} \underline{A}. \quad (2.21)$$

The variation in dielectric potential energy is

$$\delta\mathcal{V}_{dielectric} = \delta\underline{q}' \left\{ \int_{V_{ol}} \underline{\Phi}_D \epsilon^{-1} \underline{\Phi}_D' dV_{ol} \right\} \underline{q}. \quad (2.22)$$

The variation in external work is

$$\delta\mathcal{W}^{ext} = \delta\underline{A}' \underline{\Phi}_u f' + \delta\underline{q}' V', \quad (2.23)$$

where $\underline{\Phi}_u$ is evaluated at the location of the applied force. Next we define the mass, stiffness matrices, the coupling vector, and the inverse of the capacitance as the following integrals,

$$\begin{aligned} \mathbf{M}_s &= \int_{V_{ol}} \rho \underline{\Phi}_u \underline{\Phi}_u' dV_{ol} & \mathbf{K}_s &= \int_{V_{ol}} (L_u \underline{\Phi}_u)' \mathbf{c} L_u \underline{\Phi}_u' dV_{ol} \\ \underline{\Psi} &= - \int_{V_{ol}} (L_u \underline{\Phi}_u)' \mathbf{h} \underline{\Phi}_D' dV_{ol} & \mathbf{C}^{-1} &= \int_{V_{ol}} \underline{\Phi}_D \epsilon^{-1} \underline{\Phi}_D' dV_{ol} \end{aligned}, \quad (2.24)$$

Applying Hamilton's Principle yields

$$\delta\underline{A}' \left(-\mathbf{M}_s \ddot{\underline{A}} - \mathbf{K}_s \underline{A} - \underline{\Psi} \underline{q} + \underline{\Phi}_u f' \right) + \delta\underline{q}' \left(-\underline{\Psi}' \underline{A} - \mathbf{C}^{-1} \underline{q} + V' \right) = 0, \quad (2.25)$$

where $\underline{\Phi}_u$ is evaluated at the point of force application. For arbitrary variations the terms in parenthesis must be equal to zero for the equality to be satisfied. The resulting equations are placed in matrix form

$$\begin{bmatrix} \mathbf{M}_s & 0 \\ 0 & 0 \end{bmatrix} \begin{Bmatrix} \ddot{\underline{A}} \\ \ddot{\underline{q}} \end{Bmatrix} + \begin{bmatrix} \mathbf{K}_s & \underline{\Psi} \\ \underline{\Psi}' & \mathbf{C}^{-1} \end{bmatrix} \begin{Bmatrix} \underline{A} \\ \underline{q} \end{Bmatrix} = \begin{Bmatrix} \underline{\Phi}_u f' \\ V' \end{Bmatrix}. \quad (2.26)$$

At this point the model appears to be very different from Hagood's as the matrix is symmetric. This is because we chose both generalized coordinates to be the displacement terms while Hagood chose one forcing term and one displacement term resulting in a skew-symmetric matrix. The other major difference is the method we chose to solve the equations. Hagood placed the equations in state space form before solving them. Our method allows the introduction of the frequency dependent material properties thus the elements of the matrices given in Equation 2.24 are rewritten to include the frequency dependence,

$$\begin{aligned} \mathbf{M}_s &= \int_{V_{ol}} \rho \underline{\Phi}_u \underline{\Phi}_u' dV_{ol} & \mathbf{K}_s(j\omega) &= \int_{V_{ol}} (L_u \underline{\Phi}_u)' \mathbf{c}(j\omega) L_u \underline{\Phi}_u' dV_{ol} \\ \underline{\Psi}(j\omega) &= - \int_{V_{ol}} (L_u \underline{\Phi}_u)' \mathbf{h}(j\omega) \underline{\Phi}_D' dV_{ol} & \mathbf{C}^{-1}(j\omega) &= \int_{V_{ol}} \underline{\Phi}_D \epsilon^{-1}(j\omega) \underline{\Phi}_D' dV_{ol} \end{aligned}, \quad (2.27)$$

and the second order differential equation given by Equation 2.26 is transformed to the frequency domain by assuming harmonic forcing functions \underline{f} and \underline{V} .

$$\begin{bmatrix} -\mathbf{M}_s\omega^2 + \mathbf{K}_s(j\omega) & \underline{\Psi}(j\omega) \\ \underline{\Psi}'(j\omega) & \mathbf{C}^{-1}(j\omega) \end{bmatrix} \begin{Bmatrix} \underline{A}(j\omega) \\ \underline{q}(j\omega) \end{Bmatrix} = \begin{Bmatrix} \underline{\Phi}_u \underline{f}'(j\omega) \\ \underline{V}(j\omega)' \end{Bmatrix}, \quad (2.28)$$

We then evaluate the matrix for each frequency of interest and then solve for the generalized coordinates through matrix inversion. Once the generalized coordinates are solved for they can be substituted back into Equation (2.13) resulting in the displacements.

2.4 Chapter Summary

In this chapter we have shown the development of a potential energy function which is valid for an electro mechanically coupled dielectric material. We then wrote the kinetic and potential energy functions as well as the external work in terms of generalized displacement coordinates. The variational method and Hamilton's principal yielded a second order matrix differential equation. The differential equation was then transformed into the frequency domain and the frequency dependence of the material properties was reintroduced.

Chapter 3

Cantilever Beam Example and Material Characterization

In the previous chapter we developed a variational model of a general ionic polymer-based structure. In this chapter we will demonstrate the method as applied to an Euler Bernoulli cantilever beam. We will evaluate the second row of Figure 2.1 including loading and boundary conditions, and the shape functions. A very important section of this chapter provides a method of characterizing the material properties. After these properties are determined simulations of both actuation and sensing response are compared to experimental results and the modeling method is shown to be valid.

3.1 Assumptions and Simplifications

The model geometry is shown in Figure 3.1. Several assumptions which are reasonable for this geometry can be applied to simplify the generalized formulation. First, we only consider mechanical and electrical displacements in the X_3 direction. While there may be some small displacements in other directions they are considered negligible. This assumption reduces the displacement vectors to scalars ($\underline{U} = U_3$, $\underline{D} = D_3$). An additional result of this is that the permittivity matrix (ϵ) is reduced to the scalar ϵ_{33} . The cantilever is long and slender

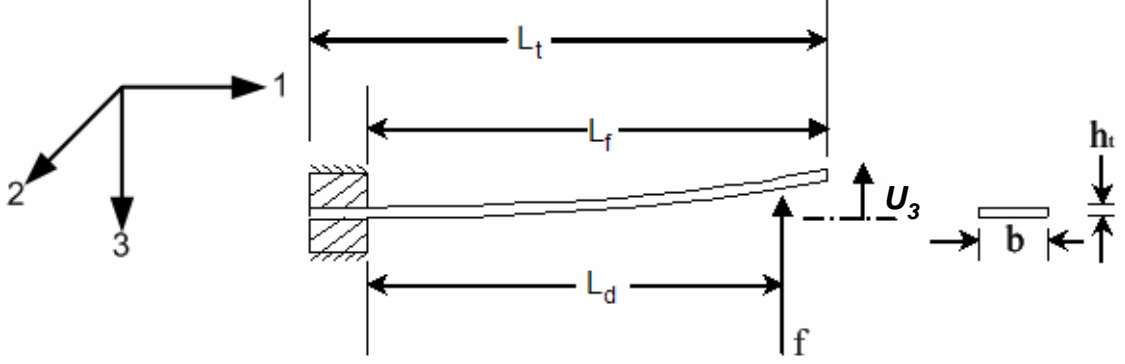


Figure 3.1: Transducer geometry

so we apply Euler-Bernouli small deflection assumptions, therefore,

$$L_u = z \begin{Bmatrix} \frac{\partial^2}{\partial X_1^2} \\ -\nu \frac{\partial^2}{\partial X_1^2} \\ -\nu \frac{\partial^2}{\partial X_1^2} \end{Bmatrix} \quad \text{and} \quad \mathbf{c}^D = \frac{Y}{(1+\nu)(1-2\nu)} \begin{bmatrix} 1-\nu & \nu & \nu \\ \nu & 1-\nu & \nu \\ \nu & \nu & 1-\nu \end{bmatrix} \quad (3.1)$$

where Y is simply the tensile modulus. We have assumed that the mode shapes of an uncoupled beam are good approximations for our shape functions. These mode shapes can be found, in most vibration texts such as those by Inman (Inman, 2001) or Blevins (Blevins, 1995), to be

$$\Phi_{un} = \cosh(\beta_n X_1) - \cos(\beta_n X_1) - \sigma_n [\sinh(\beta_n X_1) - \sin(\beta_n X_1)], \quad (3.2)$$

where β_n and σ_n are also listed in vibration texts. There is only one electrode on each side of the polymer so $\underline{V}(\underline{X}) = V$. Electric displacement is constant and all the charge is present on the surface resulting in

$$\Phi_{D\ upper} = \frac{1}{bL_t} \quad \text{and} \quad \Phi_{D\ lower} = \frac{-1}{bL_t}. \quad (3.3)$$

The shape functions of Equation 3.2 are orthogonal to each other, therefore carrying out the integrations shown in Equation 2.24 results in diagonal \mathbf{M}_s and \mathbf{K}_s matrices. Because the voltage is constant over the single electrode, the $\underline{\Psi}$ vector is a column vector, and \mathbf{C}^{-1} is a scalar. The elements are

$$\begin{aligned} M_{nn} &= \rho b h_t L_f \\ K_{nn} &= \frac{1}{12} Y b h_t^3 L_f \beta_n^4 \\ \Psi_{n1} &= -h_{13} \frac{h_t^2}{2L_t} \int_0^{L_f} X_{n,xx}(x) dx \\ C^{-1} &= \frac{h_t}{\epsilon_{33}^T b L_t} \end{aligned} \quad (3.4)$$

Finally, the matrices of Equation 2.28 is developed for for each frequency of interest and the generalized coordinates are solved for through matrix inversion as in Equation (3.5)

$$\begin{Bmatrix} \underline{A}(j\omega) \\ \underline{q}(j\omega) \end{Bmatrix} = \begin{bmatrix} -\mathbf{M}_s\omega^2 + \mathbf{K}_s(j\omega) & \underline{\Psi}(j\omega) \\ \underline{\Psi}'(j\omega) & \mathbf{C}^{-1}(j\omega) \end{bmatrix}^{-1} \begin{Bmatrix} \underline{\Phi}_u f'(j\omega) \\ \underline{V}'(j\omega) \end{Bmatrix}. \quad (3.5)$$

3.2 Actuator and Sensor Equations

Our choice of the symmetric form allows a direct determination of the generalized coordinates related to displacements. This allows us to determine the operational deflections for an actuator due to a voltage input. Once the generalized coordinates are determined the displacement at any point is found by substituting $\underline{A}(j\omega)$ back into Equation (2.13).

To use this method to model sensors we assume that there is a single electrode and the force is only applied at one point which reduces the charge and voltage and force vectors to a single element each. The symmetric configuration allows charge to be used as a sensor output given a force input by setting the voltage to zero. This is reasonable because signal conditioning circuits measure short circuit charge. If voltage is the desired sensing parameter then by assuming that the instrumentation has a high impedance input we can set the charge coordinate \underline{q} in Equation (2.28) to zero and solve for the electric potential due to the force. This results in

$$\frac{V(j\omega)}{f(j\omega)} = \underline{\Psi}'(-\mathbf{M}_s\omega^2 + \mathbf{K}_s(j\omega))^{-1} \underline{\Phi}'_u. \quad (3.6)$$

The sensor equations can also be determined for a displacement input by multiplying by the previously developed equations by the transducer stiffness

$$\frac{V(j\omega)}{U(j\omega)} = \frac{V(j\omega)}{f(j\omega)} \frac{f(j\omega)}{U(j\omega)} \quad \frac{q(j\omega)}{U(j\omega)} = \frac{q(j\omega)}{f(j\omega)} \frac{f(j\omega)}{U(j\omega)} \quad (3.7)$$

This transfer function multiplication is again performed frequency by frequency resulting in the new transfer functions.

3.3 Material Characterization

The modeling method demonstrated in the previous sections is dependent on a priori knowledge of three material properties. These properties include the elastic modulus, which has

been shown to include viscoelastic effects, the dielectric permittivity, which is not purely capacitive like a piezoelectric device, and the strain coefficient, which again is frequency dependent (Newbury and Leo, 2003b).

The material parameters are extracted from three transfer functions experimentally determined by testing cantilever beam samples. Newbury showed that the coupling in ionic polymer materials is low enough that the electrical impedance is not affected by mechanical boundary conditions nor is mechanical impedance affected by electrical boundary conditions (Newbury and Leo, 2003b). This is contrary to many other electro-mechanically coupled materials such as piezoceramics. Because of this low coupling the mechanical stiffness is only a function of transducer geometry, mass, and elastic modulus. The dielectric permittivity is the capacitance, but normalized to transducer geometry. Again, because of the low coupling the electrical impedance is only a function of transducer geometry and dielectric permittivity. Therefore, dielectric permittivity can be determined from voltage-current transfer functions (electrical impedance). Finally, the strain coefficient is determined from free deflection tests. Free deflection is a function of all three parameters so accurate estimates of the modulus and permittivity are essential to obtain accurate estimates of the strain coefficient.

3.3.1 Experimental Setup

A cantilever beam transducer of dimensions $38\text{mm} \times 3\text{mm} \times 0.3\text{mm}$ is manufactured using a multi step process. A Li^+ cation is the mobile ion and EmI-Tf ionic liquid is the solvent. The electrode is created with RuO_2 and NafionTM. The outer electrode is gold leaf, which is hot pressed onto the sample. This method of manufacture was recently developed by Akle, Bennett, and Leo, and has been shown to result in high strain air-stable actuators and sensors (Akle et al., 2004). This sample is used for both material characterization and validation of the modeling method.

The mechanical stiffness of the sample is obtained by measuring the frequency response between a force input and a displacement output. The test configuration is depicted in Figure 3.2. A random signal is generated by SigLab model 20-42 signal analyzer and amplified to excite the Bruel & Kjaer Type 4810 shaker. The displacement is measured using a Polytec OFV-303 laser vibrometer. Force is measured using a Transducer Techniques 10 gram strain gage load cell. This sliding-pinned beam configuration was previously found to

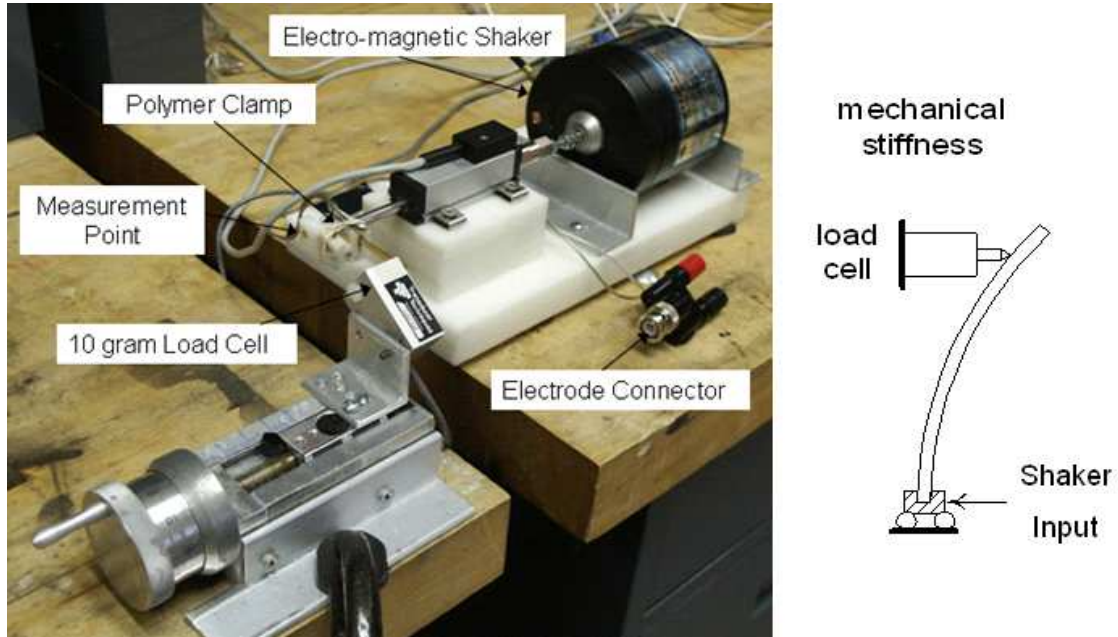


Figure 3.2: Modulus and electrical impedance test setup

reduce the effect of load cell dynamics on the measurement. Additionally, the first bending mode does not appear in the transfer function when force is measured at the pinned end thus increasing the frequency range for which resonant effects do not affect the measurement (Franklin, 2003). The Fourier analyzer averaged fifty measurements and calculated the frequency response. On both sides of the polymer clamp are electrical contacts. To verify that electrical boundary conditions do not affect the mechanical impedance tests were performed both with the contacts shorted as well as with the contacts left open.

To measure electrical impedance a random 200 mVrms signal is generated and applied to the contacts within the polymer clamp. The applied voltage and current are recorded and twenty averages are used to determine the impedance transfer function. To demonstrate that mechanical boundary conditions do not affect the electrical impedance the measurement was performed with the tip blocked as in Figure 3.2, and with the tip free as shown in Figure 3.3.

Tip deflection measurements are also performed with the experimental setup shown in Figure 3.3. In addition to measuring deflections at the tip, the deflection at seventeen additional points along the length are measured to determine the operational deflection shapes. To ensure the measurements are taken at known distances and the boundary conditions remained the same for each measurement the clamp is attached to a graduated

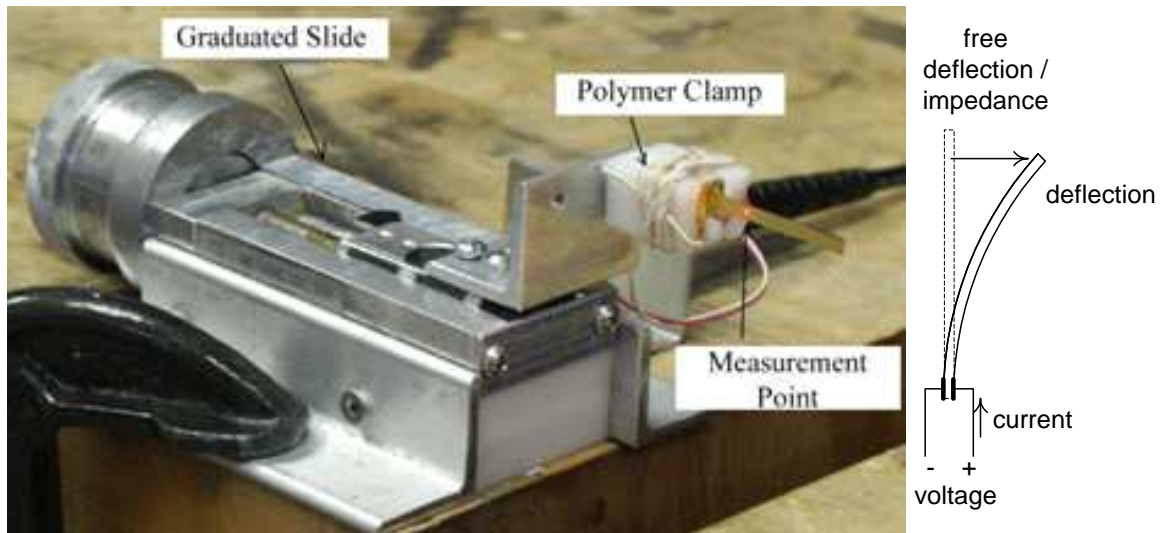


Figure 3.3: Free deflection test setup

slide and advanced forward a known distance resulting in the laser striking a point closer to the root of the beam. Measurements are taken in 2 mm increments until the distance from the root became 6mm at which point the measurements were taken in 1mm increments.

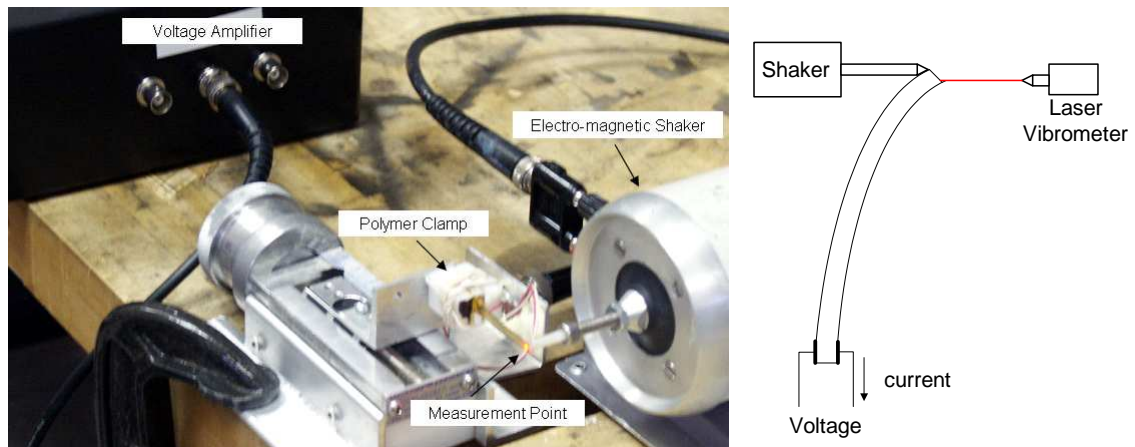


Figure 3.4: Displacement sensing test setup

The sensing properties of the transducer are investigated by displacing the tip of the cantilever beam and measuring the voltage across the beam as shown in Figure 3.4. A random signal is output from the Fourier analyzer and applied to a Ling Dynamic Systems V203 shaker. The displacement is measured using the laser vibrometer. The voltage response to the displacement input is measured using fifty averages.

3.3.2 Material Parameter Estimation

Measured mechanical stiffness data is shown in Figure 3.5. The data includes a test with both open circuit and shorted electrical boundary conditions. The variation between the open circuit and short circuit test is negligible. This validates the assumption that the difference between the short circuit and open circuit modulus is negligible even at higher frequencies.

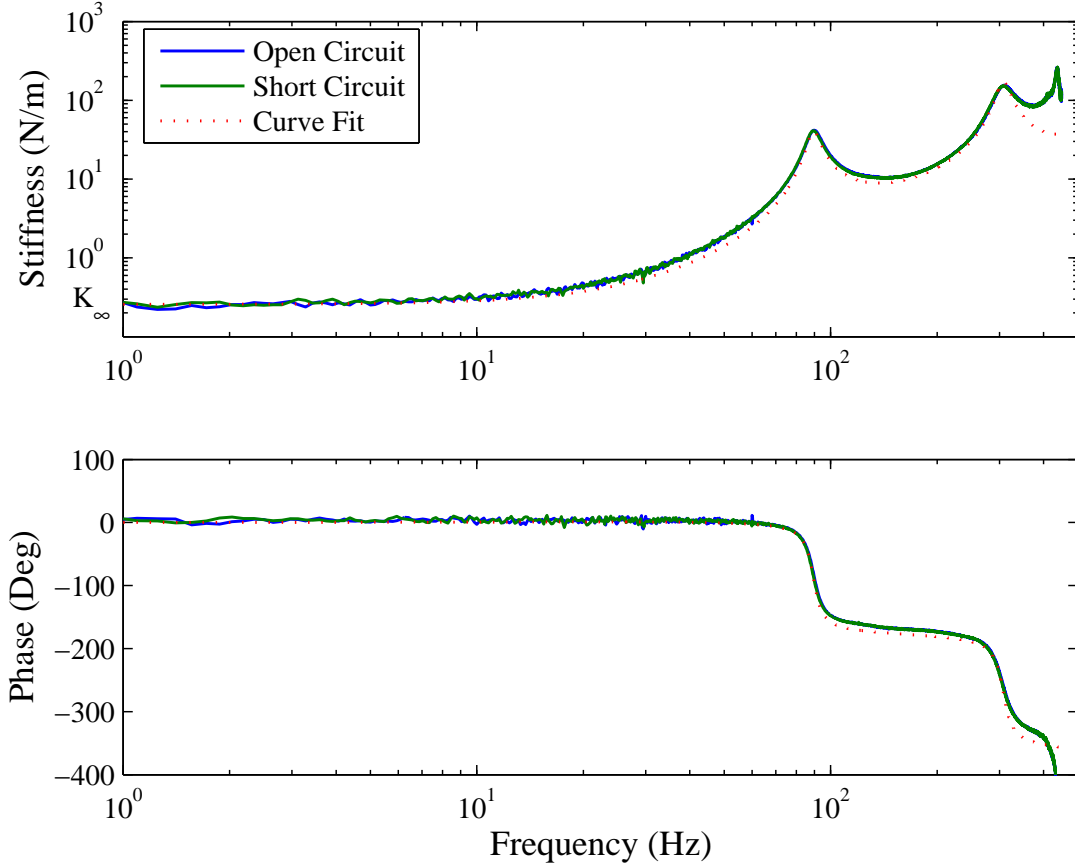


Figure 3.5: Mechanical stiffness measurements and curve fit

The elastic modulus is determined from the mechanical stiffness measurements by modeling the stiffness using Golla-Hughes McTavish (GHM) model for the viscoelasticity,

$$Y(s) = Y_{\infty} \left\{ 1 + \alpha \frac{s^2 + 2\hat{\zeta}\hat{\omega}s}{s^2 + 2\hat{\zeta}\hat{\omega}s + \hat{\omega}^2} \right\}, \quad (3.8)$$

where Y_{∞} is the static modulus, s is the Laplace variable, and α , $\hat{\zeta}$, and $\hat{\omega}$ are parameters related to the material loss (McTavish and Hughes, 1993). The static modulus is found by

determining the low frequency asymptote (K_∞) of the stiffness frequency response. At low frequency the dynamics of the beam are negligible so the static modulus derived from the static stiffness of the sliding-pinned beam is (Gere and Timoshenko, 1997)

$$Y_\infty = \frac{K_\infty L_f^3}{3I} \quad (3.9)$$

To determine the remaining GHM parameters, consider that the dynamic beam stiffness which was stated in Equation 1.3, but is repeated here for convenience.

$$K(s) = \frac{1}{\sum_{k=1}^n \frac{1}{M_k s^2 + K_k}} \left\{ Y(s) I \sum_{k=1}^n \frac{\Phi_{k,xxx}}{M_k s^2 + K_k} \right\},$$

where $\Phi_{k,xxx}$ is the third spatial derivative of the sliding-pinned mode shape, $M_k = \rho b h L_f$, and $K_k(s) = Y(s) I L_f \beta_k^4$. β_k is the weighted natural frequency corresponding to a sliding-pinned beam (Blevins, 1995). Simulations are then performed using reasonable initial guesses for α , $\hat{\zeta}$, and $\hat{\omega}$ of Equation 3.8. A constrained optimization routine is then employed, to achieve the best fit to the experimental data.

Figure 3.5 shows the curve fit achieved for this study. The curve fit slightly under predicts the damping shown in the experiment, however the error is very small as indicated in Table 3.1. Additionally, the experiment suggests there is a third peak in the frequency band studied. However, the third peak occurs at a much lower frequency than would be expected and has been determined to be an artifact created by a load cell resonance. Damped natural frequencies and damping ratios were determined from both the experiment and simulation using circle fitting (Inman, 2001). The results are summarized in Table 3.1.

Table 3.1: Comparison of Resonance and Damping Parameters

Parameter	Resonance 1	Resonance 2
ω_d Experimental (Hz)	89.85	306.7
ω_d Simulation (Hz)	89.53	307.9
Error (%)	0.1	0.39
ζ Experimental (%)	5.04	7.28
ζ Simulation (%)	4.36	4.49
Difference (%)	0.68	2.79

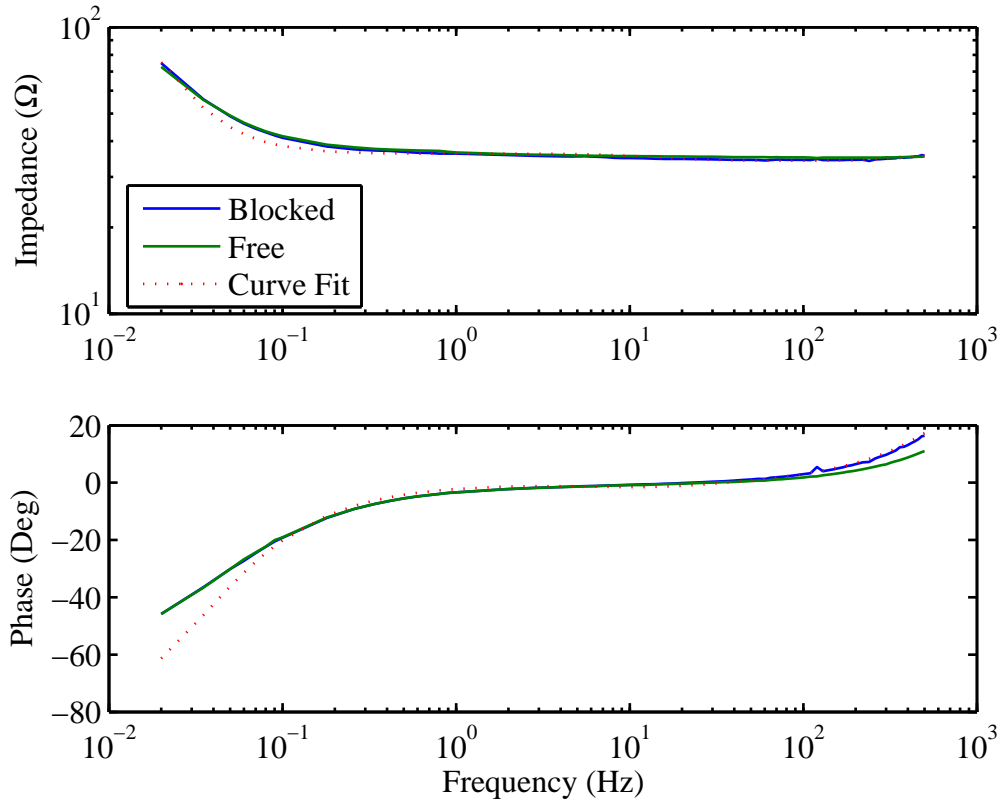


Figure 3.6: Electrical impedance measurements

The electrical impedance measurements also support the assumption that the effect of boundary conditions on impedance is negligible. Two measurements as well as a curve fit are shown in Figure 3.6. There is some variation in the measurements at higher frequency, but it is on the order of 1%, and has been considered negligible. It is also interesting that the impedance is capacitive at lower frequency as indicated by the decrease in magnitude that occurs with frequency. However, there is a high frequency asymptote in the impedance so at high frequency the material is similar to a resistor.

To extract the dielectric permittivity the capacitance is determined from the measured electrical impedance

$$C(j\omega) = \frac{1}{j\omega Z_{cap}(j\omega)}, \quad (3.10)$$

where $Z_{cap}(j\omega)$ is the measured electrical impedance as shown in Figure 3.6. The equivalent dielectric permittivity is found by normalizing capacitance to transducer geometry

$$\epsilon(j\omega) = \frac{C(j\omega)h_t}{bL_t}. \quad (3.11)$$

Substituting Equation 3.10 into the expression for permittivity results in

$$\epsilon(j\omega) = \frac{h_t}{bL_t j\omega Z_{cap}(j\omega)}. \quad (3.12)$$

The experimental data is processed as shown above and then a transfer function is fit to the result.

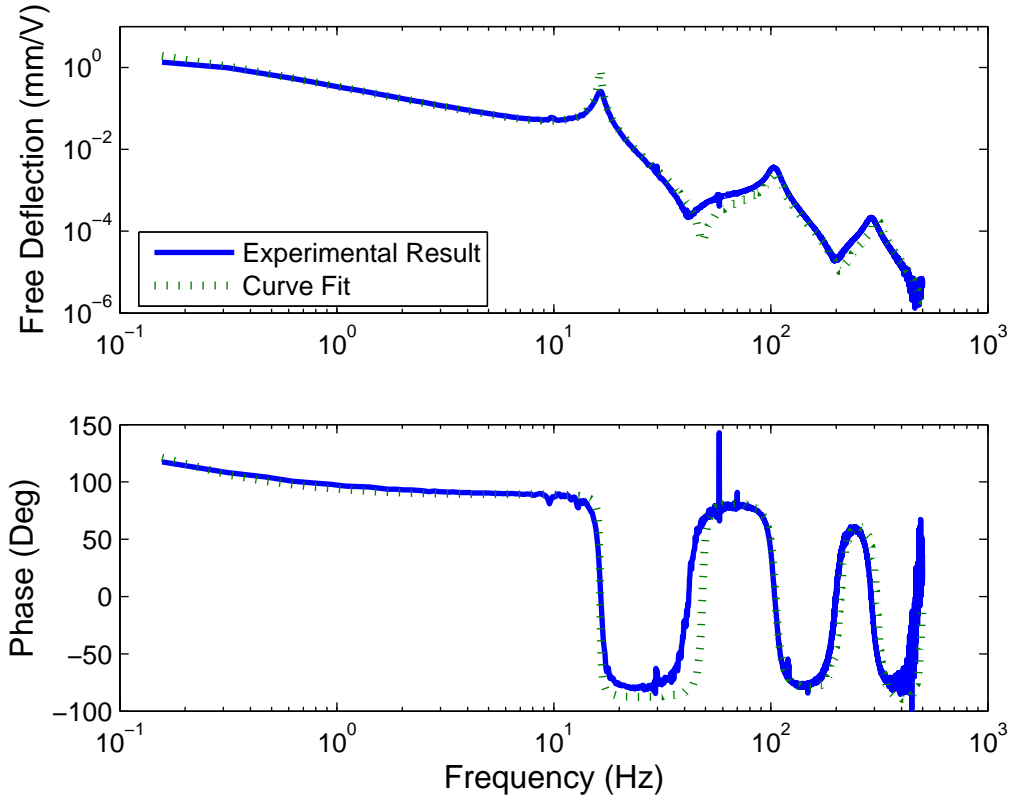


Figure 3.7: Free deflection at the actuator tip

After fitting models of modulus and permittivity to the data transfer functions for the strain coefficient are created and adjusted in models of free deflection until a good fit is achieved. Experimental data as well as a simulation are shown in Figure 3.7. The simulation agrees with the measured data reasonably well though the first anti-resonance occurs at a slightly different frequency than the simulation predicts. Also the simulated second resonance appears to be slightly more damped than the actual system. This is attributed to small inaccuracies in the modulus characterization.

3.3.3 Identified Material Properties

The results of the material characterization are summarized in Figure 3.8. The magnitude of the modulus begins to increase at about 80 Hz so additional damping is expected above this point. The strain coefficient transfer function consists of one zero and three poles. This results in roll off which increases at less than 1 Hz. The dielectric permittivity rolls off at a nearly constant rate through the frequency range studied. For convenience the transfer functions are listed below their respective plots.

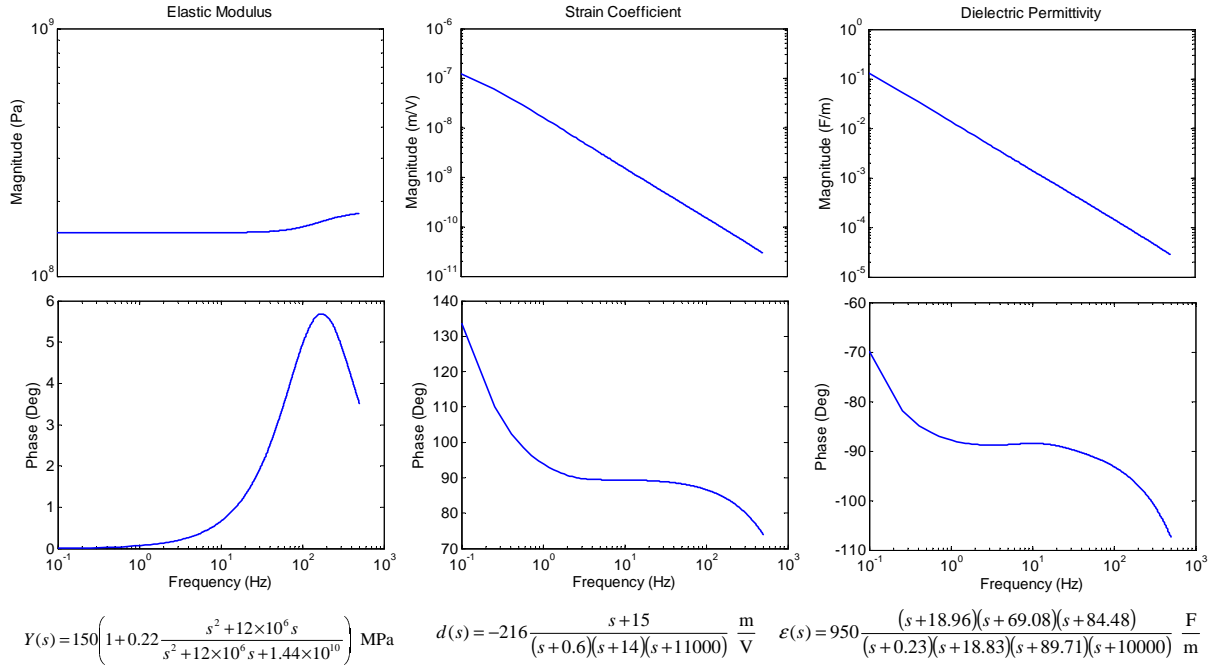


Figure 3.8: Complex Material Parameters 0.1Hz - 500Hz

3.4 Model Validation

To validate both the material model as well as the modeling method we simulated the free deflection at additional spatial points along the beam and compared the simulated transfer functions to experimental data. There are several features of these simulations that are interesting. First, we expect the frequency of the peaks to match as well at any point along the beam as they did in the simulation of the actuator tip. This is because these peaks are related to mechanical resonance or natural frequencies which are not affected by

measurement location. The simulations should reflect this. Also, because the peaks are related to the mechanical resonance the shape of these peaks is an indicator of how well the elastic modulus has been modeled. The phase drop near the peaks is a result of the mechanical resonance, but the phase response in regions away from the peaks is an indicator of how well the permittivity and strain coefficient have been modeled.

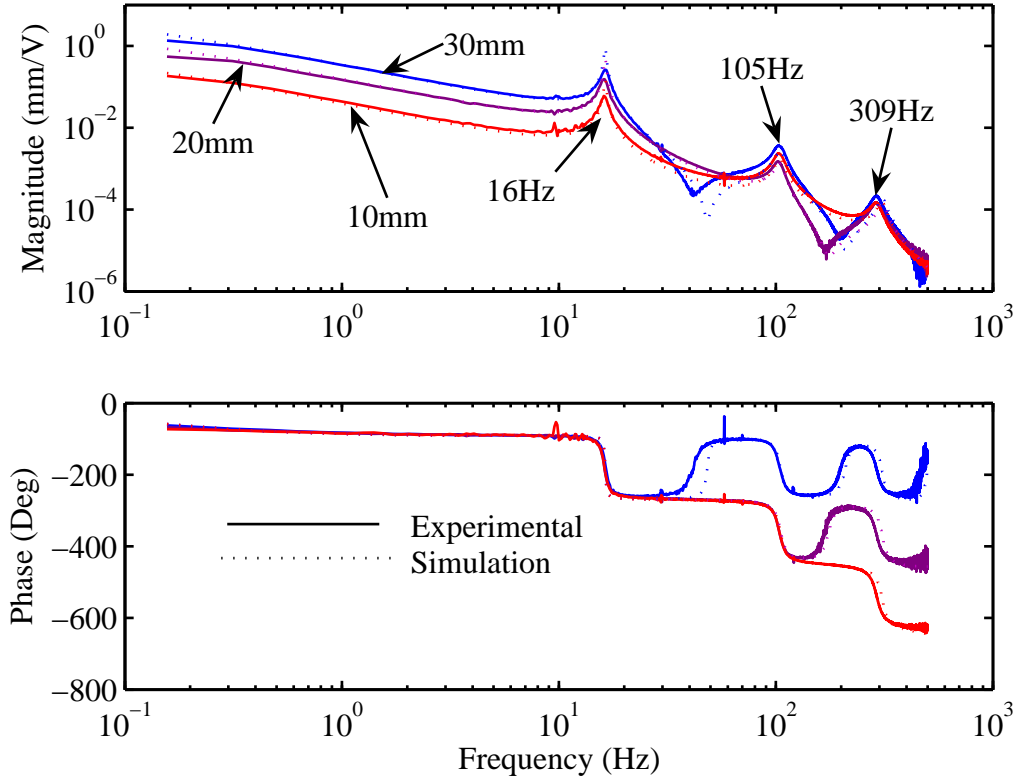


Figure 3.9: Free Deflection at three points along the actuator

The simulations are in very good agreement with the experiments. As an example, the comparison for the free deflection at three points along the actuator is shown in Figure 3.9. There is slight variation in the resonant frequencies and damping, which is attributed to under prediction of the damping in the stiffness curve fit. Also, the antiresonance associated with the tip deflection occurs at a slightly lower frequency (40 Hz rather than 50Hz) than the model predicts. This can be attributed to some uncertainty in the position of the measurement as the anti-resonant frequencies are dependent on the location of the measurement unlike the resonances which occur at the same frequency regardless of the measurement location. Finally, the phase comparisons are very encouraging. There is almost no error in

the phase plots except near the first anti-resonance. Overall, these discrepancies are very small as is summarized in Table 3.2. Notice that the phase is approximately a multiple of 90 degrees at frequencies away from the resonances. This is expected because the phase of the permittivity is approximately 90 degrees over the frequency band studied. This leads us to the conclusion that the permittivity has been modeled well.

Table 3.2: Resonance Parameters for Free Deflection

Parameter	Peak 1	Peak 2	Peak 3
ω_d Experimental (Hz)	16.4	102.9	289.8
ω_d Simulation (Hz)	16.4	104.5	308.4
Error (%)	0.003	1.5	6.4
ζ Experimental (%)	3.81	5.46	5.12
ζ Simulation (%)	0.95	5.78	5.54
Difference (%)	2.86	0.32	0.42

To show that the structural mode shapes are valid shape functions for the system, the first three transfer functions at 18 points along the beam are measured. The operational deflection shapes are then determined at the three resonances of the beam. Unlike a mechanical response the transfer functions are primarily real at the resonances because of the 90 degree phase in the permittivity. This allowed us to determine the real part of the transfer function at each point and compute the deflection shape. In Figure 3.10 the experimentally determine deflectionshape are normalized and plotted with (*), the model prediction is also normalized and shown with (+), and the shape functions are shown with a solid line.

There is excellent agreement between all three curves with the exception of some error near the root of the beam in the third mode. This is possibly because the boundary condition is not a perfectly clamped condition. If some rotation is allowed a slightly higher deflection would be expected. The effect is more pronounced in the third mode because the strain near the root is highest at the third mode.

The final study is to compare the measured sensing response to the model predictions. The voltage output of the transducer due to a mechanical displacement imposed on the tip is measured. The transfer function is calculated and is plotted with along with the

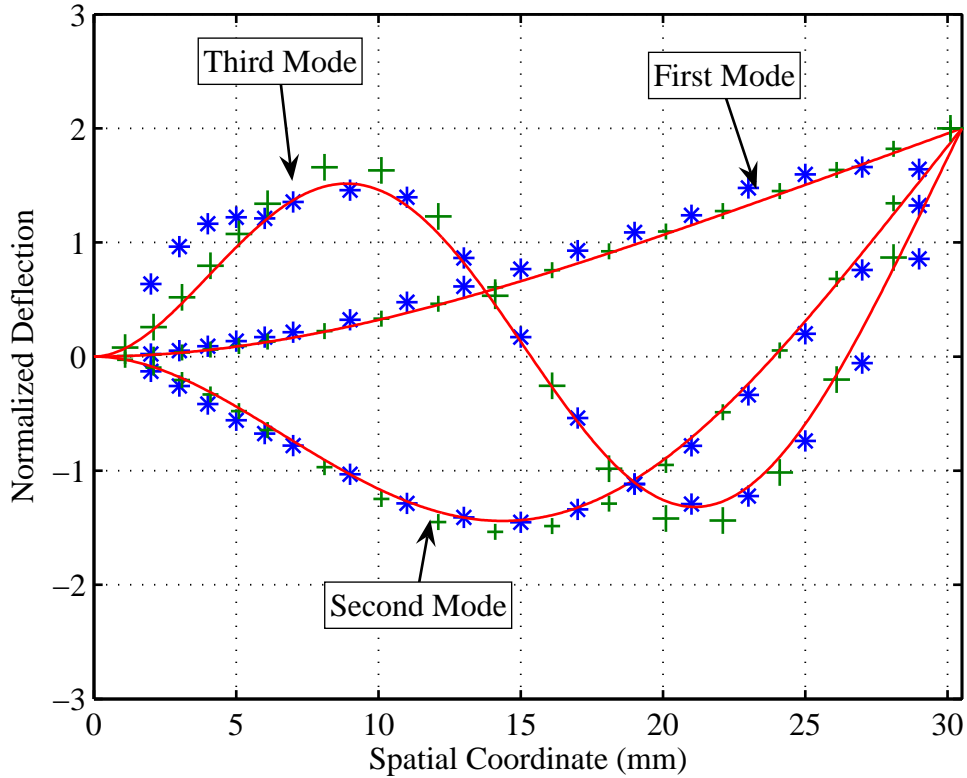


Figure 3.10: Comparison of deflection shape to structural mode-shapes

experimental results in Figure 3.11. The general shape of the transfer function is modeled very well. There is some disagreement below approximately 2 Hz. However, this error is attributed to ac coupling the signals in the experiment. The model also slightly under predicts the response near transfer function near the peaks. This is possibly due to some error in the modulus measurement or error in the position of the shaker attachment.

3.5 Chapter Summary

The work demonstrated in this chapter makes several major contributions to the modeling of ionomeric polymers. First, it demonstrates a method of modeling both actuation and sensing response of ionic polymer devices over a larger frequency range than previous work. While previous model were useful for both sensing and actuating devices they were not validated above the first resonant frequency. Second, it demonstrates that the variational principle can be used to model ionic polymers. Earlier work showed that the method

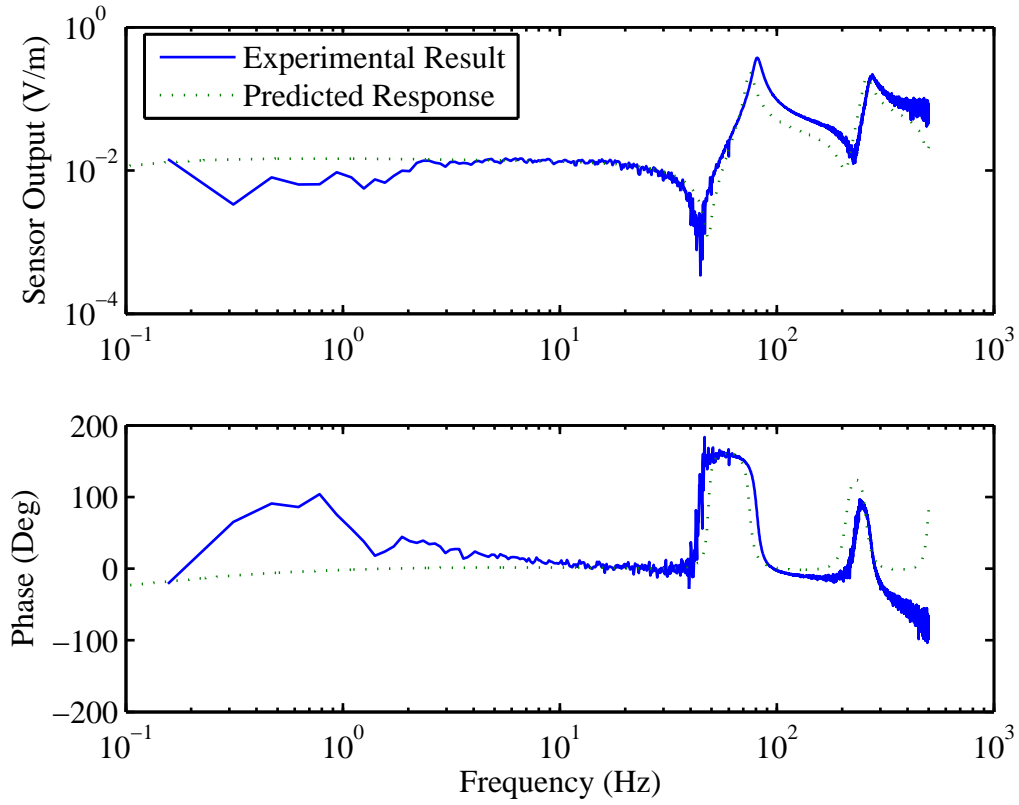


Figure 3.11: Comparison experimental sensing response to the model

could be applied to purely dielectric materials such as piezo-ceramics, but this work showed that the potential energy function can be used along with frequency dependent properties to model the behavior ionic polymers. Finally, because the modeling method is useful for a larger frequency range than previous methods, characterization techniques originally developed by Newbury and Franklin have been expanded to higher frequencies as well.

Chapter 4

Plate Modeling and Experimental Validation

The previous chapter demonstrated the modeling method as applied to a beam, which can be modeled in a single dimension. In this chapter the same method will be applied to a plate structure, which requires modeling in two dimensions. We will also expand the potential energy function to include the effect of pre-stress and non-homogeneous boundary conditions. Experiments will be performed on a square plate which is nearly pinned at the corners, then a model will be developed which includes tension and rotational springs at the boundary to compensate for the non-ideal boundary conditions.

4.1 Plate Model in Cylindrical Coordinates

We begin our development of plate models by assuming that like the beam model both mechanical and electric displacements are limited to the direction normal (see Figure 4.1) to the plate resulting in

$$\underline{U} = U_3 \quad \underline{D} = D_3. \quad (4.1)$$

We then assume that the structure is under plane strain. This reduces the strain vector to three elements and the compliance to a 3×3 matrix (Blevins, 1995). These results are

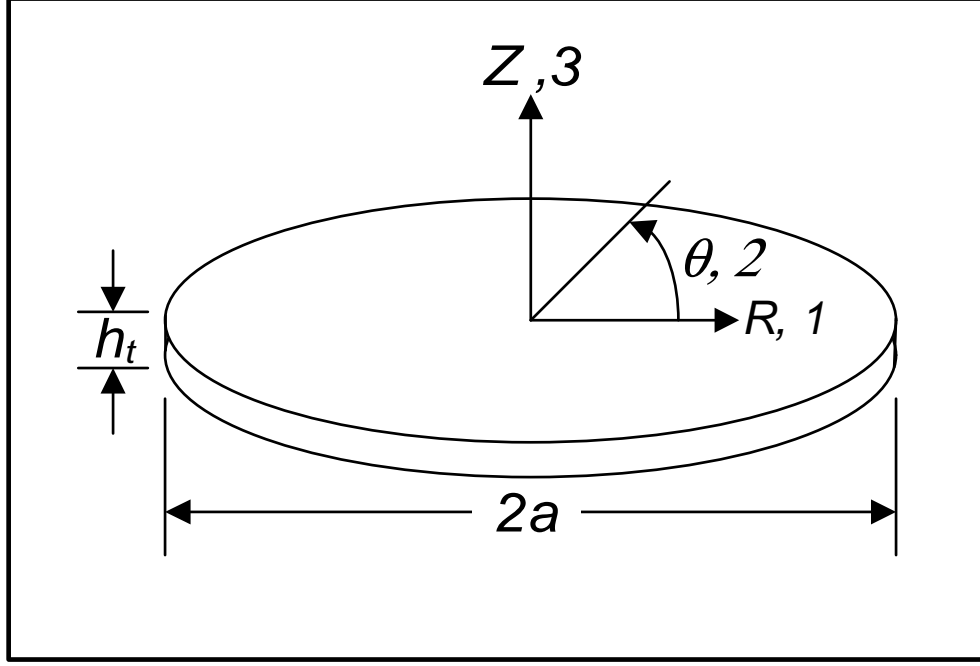


Figure 4.1: Geometry of Plate in Cylindrical Coordinates

summarized below.

$$L_u = z \left\{ \begin{array}{c} \frac{\partial^2}{\partial r^2} \\ \frac{1}{r} \frac{\partial}{\partial r^2} + \frac{1}{r^2} \frac{\partial^2}{\partial \theta^2} \\ \frac{2}{r} \frac{\partial^2}{\partial r \partial \theta} - \frac{2}{r^2} \frac{\partial}{\partial \theta} \end{array} \right\} \quad c = \frac{Y}{1 - \nu^2} \begin{bmatrix} 1 & \nu & 0 \\ \nu & 1 & 0 \\ 0 & 0 & \frac{1-\nu}{2} \end{bmatrix} \quad (4.2)$$

A set of shape functions that satisfy the boundary conditions are the structural mode shapes. They are

$$\Phi_{nk}(r\theta) = \left(J_n \left(\frac{\alpha_k r}{a} \right) - \frac{J_n(\alpha_k)}{I_n(\alpha_k)} I_n \left(\frac{\alpha_k r}{a} \right) \right) \cos(n\theta) \quad (4.3)$$

where n corresponds to the number of nodal lines in the structural mode shape and α_k are the weighted natural frequencies, which are determined by solving the transcendental equation associated with the particular boundary conditions (Blevins, 1995). Table 4.1 shows the transcendental equations for both simply supported and clamped edge boundary conditions and summarizes the weighted natural frequencies used in this analysis.

We assume the charge to be uniformly distributed on the surfaces so the electrical shape functions are

$$\Phi_D^u = \frac{1}{\pi a^2} \quad \Phi_D^l = \frac{-1}{\pi a^2} \quad (4.4)$$

Table 4.1: Weighted Natural Frequencies for Circular Plate

Simply Supported		Clamped Edge	
$\frac{J_{n+1}(\alpha)}{J_n(\alpha)} + \frac{I_{n+1}(\alpha)}{I_n(\alpha)} = \frac{2\alpha}{1-\nu}$		$\frac{J_{n+1}(\alpha)}{J_n(\alpha)} + \frac{I_{n+1}(\alpha)}{I_n(\alpha)} = 0$	
n	α	n	α
0	2.2831	0	3.1962
0	5.4722	0	6.3064
0	8.2639	0	9.4395
1	3.7604	1	4.6109
1	6.9784	1	7.7993

where a is the radius of the plate. This analysis again results in the set of matrix equations

$$\begin{bmatrix} -\mathbf{M}_s \omega^2 + \mathbf{K}_s(j\omega) & \underline{\Psi}(j\omega) \\ \underline{\Psi}'(j\omega) & \mathbf{C}^{-1}(j\omega) \end{bmatrix} \begin{Bmatrix} \underline{A}(j\omega) \\ \underline{q}(j\omega) \end{Bmatrix} = \begin{Bmatrix} \underline{\Phi}_u' \underline{f}'(j\omega) \\ \underline{V}(j\omega)' \end{Bmatrix},$$

where the elements are still defined as in equation 2.27

$$\begin{aligned} \mathbf{M}_s &= \int_{V_{ol}} \rho \underline{\Phi}_u' \underline{\Phi}_u dV_{ol} & \mathbf{K}_s(j\omega) &= \int_{V_{ol}} (L_u \underline{\Phi}_u)' \mathbf{c}(j\omega) L_u \underline{\Phi}_u dV_{ol} \\ \underline{\Psi}(j\omega) &= - \int_{V_{ol}} (L_u \underline{\Phi}_u)' \mathbf{h}(j\omega) \underline{\Phi}_D dV_{ol} & \mathbf{C}^{-1}(j\omega) &= \int_{V_{ol}} \underline{\Phi}_D' \epsilon^{-1}(j\omega) \underline{\Phi}_D dV_{ol} \end{aligned},$$

except that the integration is carried out in cylindrical coordinates.

4.1.1 Simulations of Ionic Polymer Disks

A set of circular disk simulations are shown in Figure 4.2. The material properties identified in Chapter 3 were applied to three possible configurations for a circular disk. They all three had an active component with a diameter of 34 mm and thickness of 270 μm . The simply supported and clamped edge models models included only active components. While in the passive material model, the same active component was modeled but it was encapsulated between two layers of 6 μm Mylar. They Mylar extended to a diameter of 36 mm and was modeled in a clamped configuration.

There are several advantages to simulations such as these. First, it may be desired to encapsulate the material to protect it from the environment and this method allows

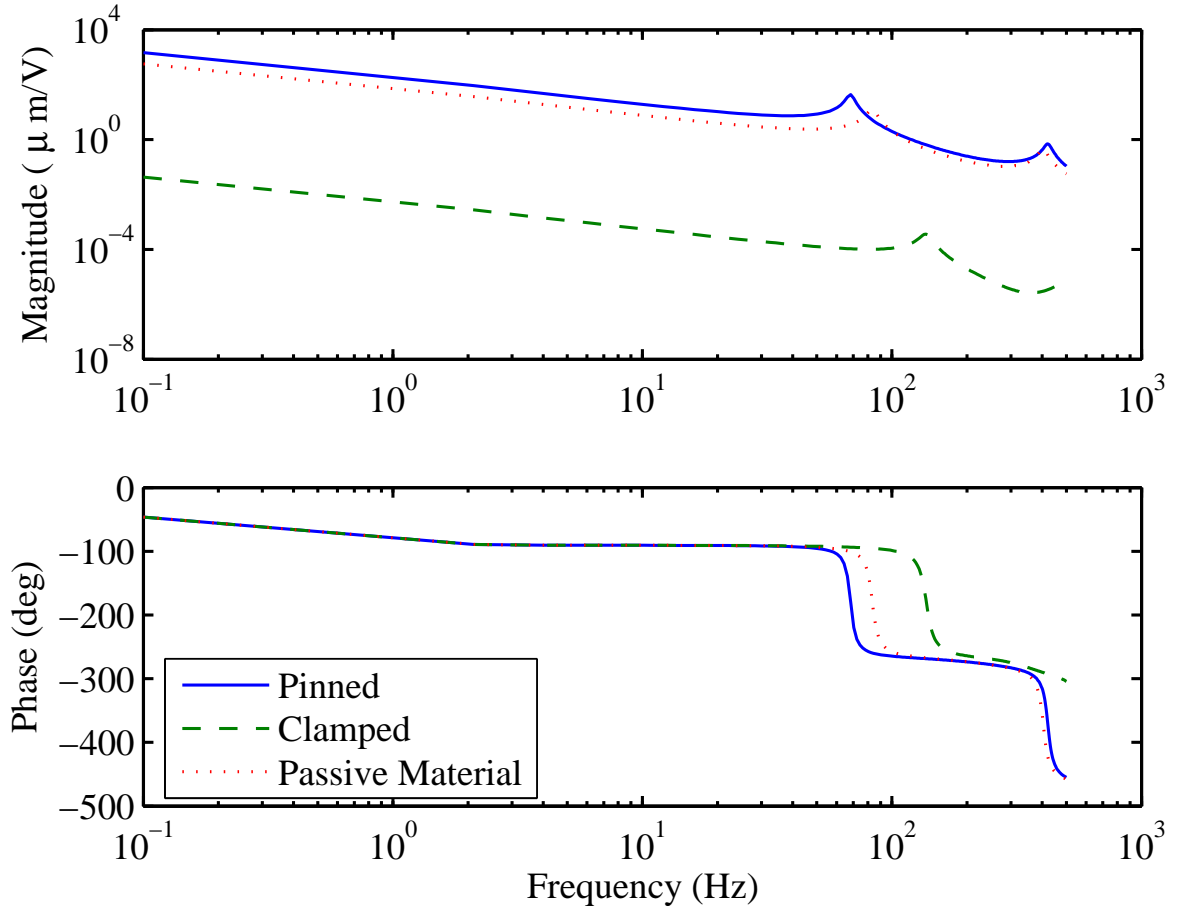


Figure 4.2: Effects of boundary conditions on center point deflection

estimation of the performance loss due to the encapsulation. Second, though the model indicates that the pinned boundary conditions result in displacements four orders of magnitude higher than the clamped boundary conditions applying the pinned conditions may be impractical. This simulation demonstrates a method of achieving displacements that are nearly equal to the displacements achieved with pinned boundary conditions.

Additionally we can simulate deflection shapes for each of the models. Figure 4.3 shows the deflection shapes of all three models at their respective resonance frequencies as well as the difference between pinned model and the model with a clamped passive material. All four plots show the x and y range associated with the passive material model; however, the pinned and clamped BC simulations have zero deflection outside the boundary diameter. As expected the pinned shape has the largest deflection at every point including the center point, which was shown in Figure 4.2. The difference between the

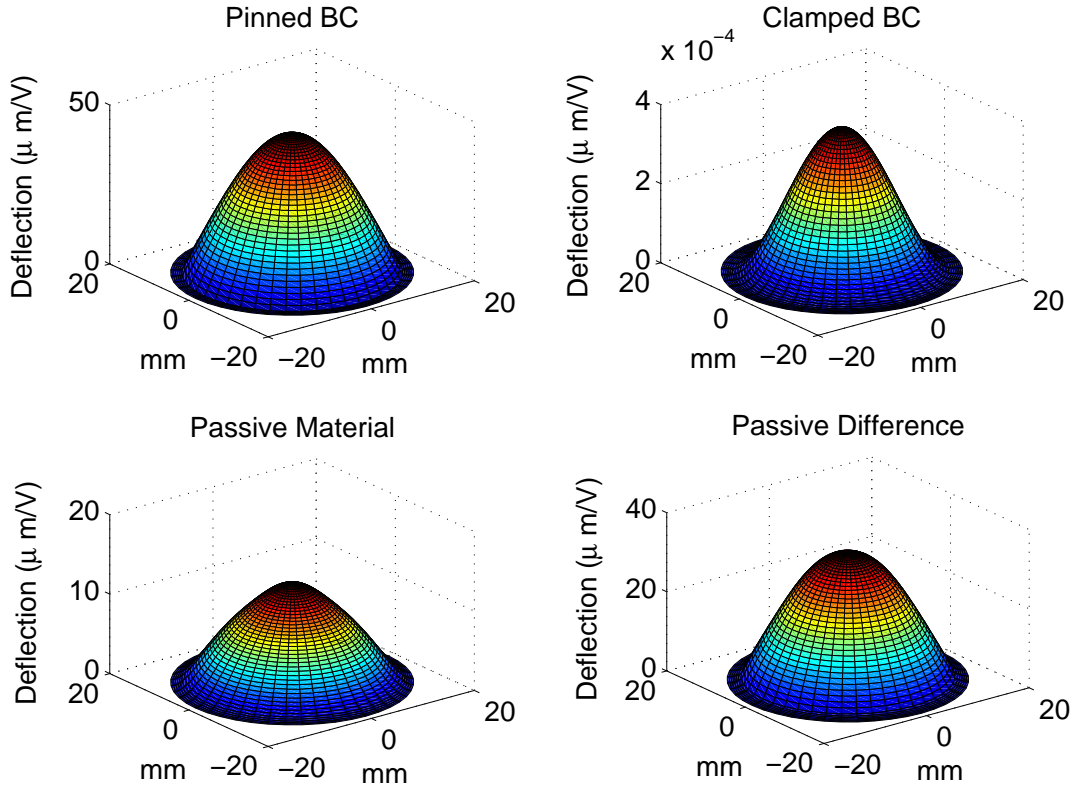


Figure 4.3: Effects of boundary conditions resonant deflection shapes

pinned model and the model including the passive material is still rather large (about a factor of 3), but it is a substantial improvement on the simulation with a clamped boundary.

The second deflection shape is possibly more interesting. Figure 4.4 shows a comparison of the pinned model and the model including the passive material at their respective 2nd resonance frequency. This is promising because the simulation predicts that the shape of the disk with a clamped passive material is very similar to the shape of a pinned disk. Figure 4.2 showed that the frequencies of these resonances was very close as well; therefore, these simulations show that we can design systems with clamped boundaries that will exhibit responses very similar to a system with a simply supported boundary.

The next section will focus on a plate model in Cartesian coordinates and will include an extensive model validation which demonstrates the validity of this method and suggests that the simulations just shown can be used for pre-prototype predictions.

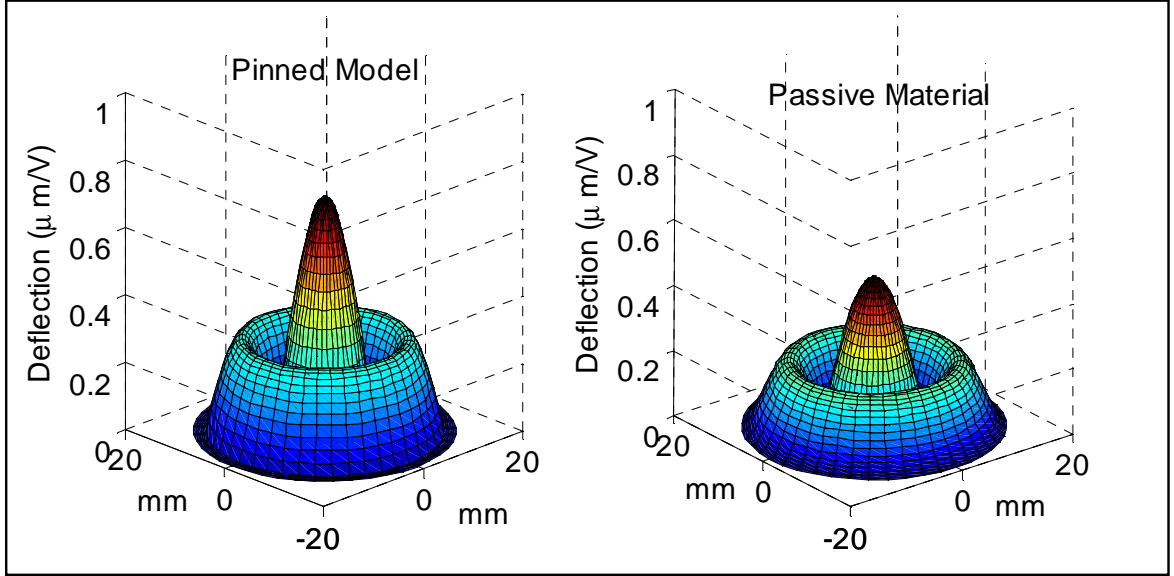


Figure 4.4: Comparison of 2nd resonant shapes

4.2 Cartesian Coordinates

The previous section demonstrated a plate model developed in cylindrical coordinates. Here we will develop a plate model in Cartesian coordinates. This model will be further extended to include the effects of an initial tension and a non-homogeneous boundary condition. We will then present some experimental results and comparisons to the simulations which provide very strong evidence that this modeling method is valid for plate structures made from ionomeric materials.

4.2.1 Expanded Potential Energy Function

The original potential energy function shown in Equation 2.2 has been expanded to allow modeling of a plate with a uniform tension (τ) and rotational springs at four corners. The potential energy associated with a uniform initial tension is uniform through the thickness and can then be treated like the potential energy due to a uniform tension in a membrane. The volumetric potential energy in a membrane is

$$\mathcal{V}_{membrane} = \frac{1}{2} \tau S'_m S_m, \quad (4.5)$$

where S_m is the strain at the neutral axis, and τ is the uniform tension per unit width. The potential energy stored in a torsional spring is

$$\mathcal{V}_{ts} = \frac{1}{2} K_{ts} \theta' \theta, \quad (4.6)$$

where K_{ts} is a torsional spring constant and θ is the angle of rotation at the spring location. The membrane potential energy is evaluated over the entire area of the plate while the potential energy in the spring is evaluated over the boundary (Ω). In this case the boundary is four discrete points at the corners. The expanded potential energy function is then

$$\mathcal{V} = \int_{Vol} \frac{1}{2} \underline{S}' \underline{c} \underline{S} - \underline{S}' \underline{h} \underline{D} + \frac{1}{2} \underline{D}' \underline{\epsilon}^{-1} \underline{D} \, dVol + \int_{Area} \frac{1}{2} \tau \underline{S}'_m \underline{S}_m \, dArea + \int_{\Omega} \frac{1}{2} K_{ts} \theta' \theta \, d\Omega \quad (4.7)$$

4.2.2 Assumptions and Development

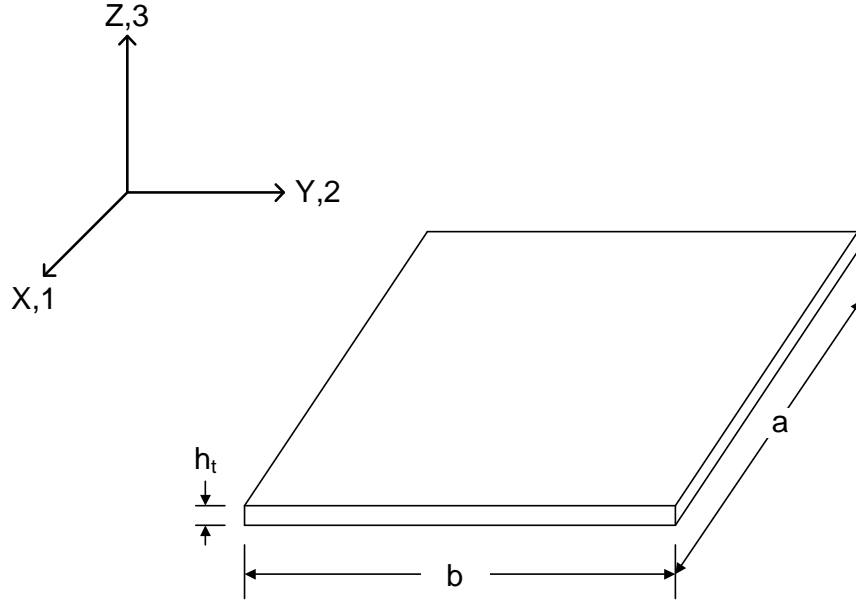


Figure 4.5: Square plate geometry used used in simulations

As in both the beam and circular plate developments we begin by making assumptions which simplify the generalized formulation. First we assume plane strain and isotropic materials so the stiffness matrix and the differential operator relating bending strain to dis-

placement are (Blevins, 1995)

$$c = \frac{Y}{1-\nu^2} \begin{bmatrix} 1 & \nu & 0 \\ \nu & 1 & 0 \\ 0 & 0 & \frac{1-\nu}{2} \end{bmatrix} \quad L_u = \begin{Bmatrix} z \frac{\partial^2}{\partial x^2} \\ z \frac{\partial^2}{\partial y^2} \\ 2z \frac{\partial^2}{\partial x \partial y} \end{Bmatrix}, \quad (4.8)$$

where Y is the tensile elastic modulus and ν is the poissons ratio which was assumed to be 0.5. Both the rotation at the boundaries and membrane strain are related to displacement through the gradient operator (Meirovitch, 1997)

$$L_{ts} = L_m = \begin{Bmatrix} \frac{\partial}{\partial x} \\ \frac{\partial}{\partial y} \end{Bmatrix}. \quad (4.9)$$

As in the beam example, we assume both electrical and mechanical displacements to be only normal to the plate or in the 3 direction as shown in Figure 4.5. Therefore, the mechanical and electrical displacement vectors are

$$\underline{U} = U_3 \quad \underline{D} = D_3 \quad (4.10)$$

A set of shape functions which fit the geometric boundary conditions contains two generalized coordinates per mode. This set of function is (Reed, 1965)

$$\phi_{u \ mn} = A_{mn} \cos\left(\frac{m\pi x}{a}\right) \sin\left(\frac{n\pi y}{b}\right) + B_{mn} \cos\left(\frac{m\pi y}{b}\right) \sin\left(\frac{n\pi x}{a}\right), \quad (4.11)$$

where m is an index running from zero to infinity which was truncated at four, and n runs from one to infinity, but was truncated at five. The length and width parameters a and b are shown in Figure 4.5. The set of shape function have two indicies so to take advantage of the matrix manipulations associated with the analysis we transformed the indexing on m and n resulting in fifty element vector of generalized coordinates for mechanical displacement.

We also continue to assume that the charge is concentrated at the surfaces and the charge on the top electrode is equal and opposite to the charge on the bottom electrode.

$$\Phi_D^u = \frac{1}{ab} \quad \Phi_D^l = \frac{-1}{ab} \quad (4.12)$$

The variational principal again results in the matrix representation of a set of linear equations which was given by equation 2.28 and is repeated here for convenience.

$$\begin{bmatrix} -\mathbf{M}_s \omega^2 + \mathbf{K}_s(j\omega) & \underline{\Psi}(j\omega) \\ \underline{\Psi}'(j\omega) & \mathbf{C}^{-1}(j\omega) \end{bmatrix} \begin{Bmatrix} \underline{A}(j\omega) \\ \underline{q}(j\omega) \end{Bmatrix} = \begin{Bmatrix} \underline{\Phi}_u' f'(j\omega) \\ \underline{V}(j\omega)' \end{Bmatrix},$$

where the components \mathbf{M}_s , \mathbf{C}^{-1} , and $\underline{\Psi}$ are defined as before and reiterated here, however because the A_{mn} terms of the shape functions are not necessarily orthogonal to the B_{mn} term the \mathbf{M}_s is not necessarily diagonal.

$$\begin{aligned} \mathbf{M}_s &= \int_{V_{ol}} \rho \underline{\Phi}_u' \underline{\Phi}_u dV_{ol} \\ \underline{\Psi}(j\omega) &= - \int_{V_{ol}} (L_u \underline{\Phi}_u)' \mathbf{h}(j\omega) \underline{\Phi}_D dV_{ol} \quad \mathbf{C}^{-1}(j\omega) = \int_{V_{ol}} \underline{\Phi}_D' \epsilon^{-1}(j\omega) \underline{\Phi}_D dV_{ol} \end{aligned} \quad (4.13)$$

The additional potential energy terms used in this development result in the stiffness matrix

$$\begin{aligned} \mathbf{K}_s(j\omega) &= \int_{V_{ol}} (L_u \underline{\Phi}_u)' \mathbf{c}(j\omega) L_u \underline{\Phi}_u dV_{ol} + \int_{Area} \tau (L_m \underline{\Phi}_u)' L_m \underline{\Phi}_u dArea \\ &\quad + \sum_{n=1}^4 K_{tsn} (L_{ts} \underline{\Phi}_u)' \mathbf{c}(j\omega) L_{ts} \underline{\Phi}_u, \end{aligned} \quad (4.14)$$

which allows a different torsional spring constant K_{tsn} at each corner.

4.2.3 Experimental Setup

A set of experiments were performed to validate the modeling approach. A square test plate was cut from the same material used in the experiments performed on the cantilever beam in the previous chapter. It was cut to be 34 mm by 34 mm; however, as shown in Figure 4.6 tabs were left on the four corners to limit the effect of the clamp on the response of the plate.

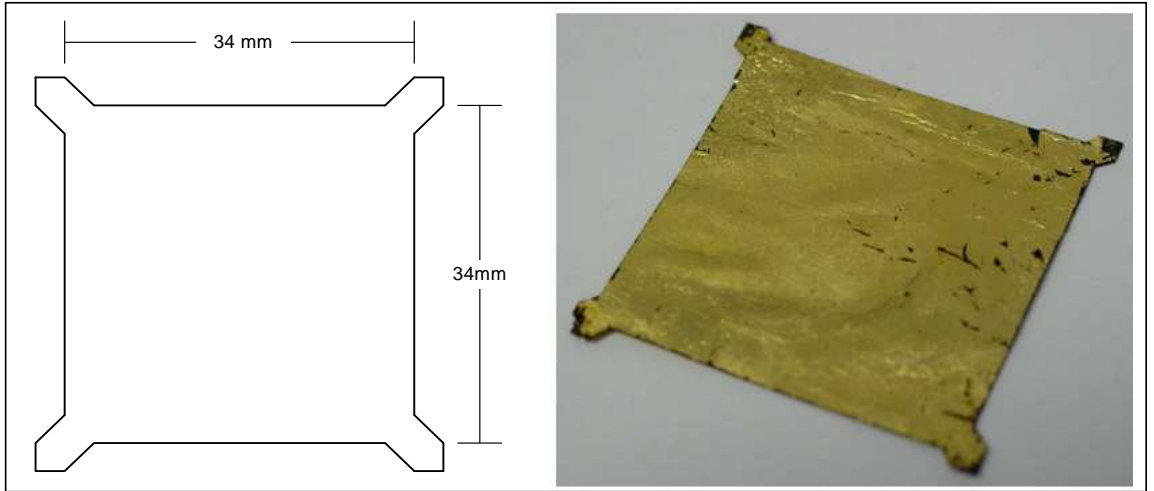


Figure 4.6: Experimental specimen geometry

The actual specimen is also shown in Figure 4.6. The dimensions are not exactly 34 mm \times 34 mm. The two dimensions average 33.5 mm \times 34.5 mm. Additionally the sample

is not completely flat. This is due to our manufacturing method. To conserve the costly ionic liquid the sample was rolled up in a vial while the ionic liquid was infused into the base polymer. While we made every effort to achieve a flat uniform sample, in the end there was some surface non-uniformity. These non-uniformities may result in localized stiffness and mass.

Next a fixture was designed and built to test the sample. This fixture which is shown in Figure 4.7 is capable of performing experiments on a square plate with dimensions ranging from 25 mm to 125 mm. Clamps with fixed electrodes are attached to sliders at the four corners and pointers on the sliders indicate the width of the plate. Though in this study a single electrode was used the fixture was built to allow a separate control channel at each quadrant of the plate. The electrical resistance of the sample electrode is very low ($\ll 1\Omega/\text{cm}$) so applying a voltage at one of the clamps should have been adequate though we applied the voltage at all four clamps to ensure a uniform voltage and subsequent charge distribution.

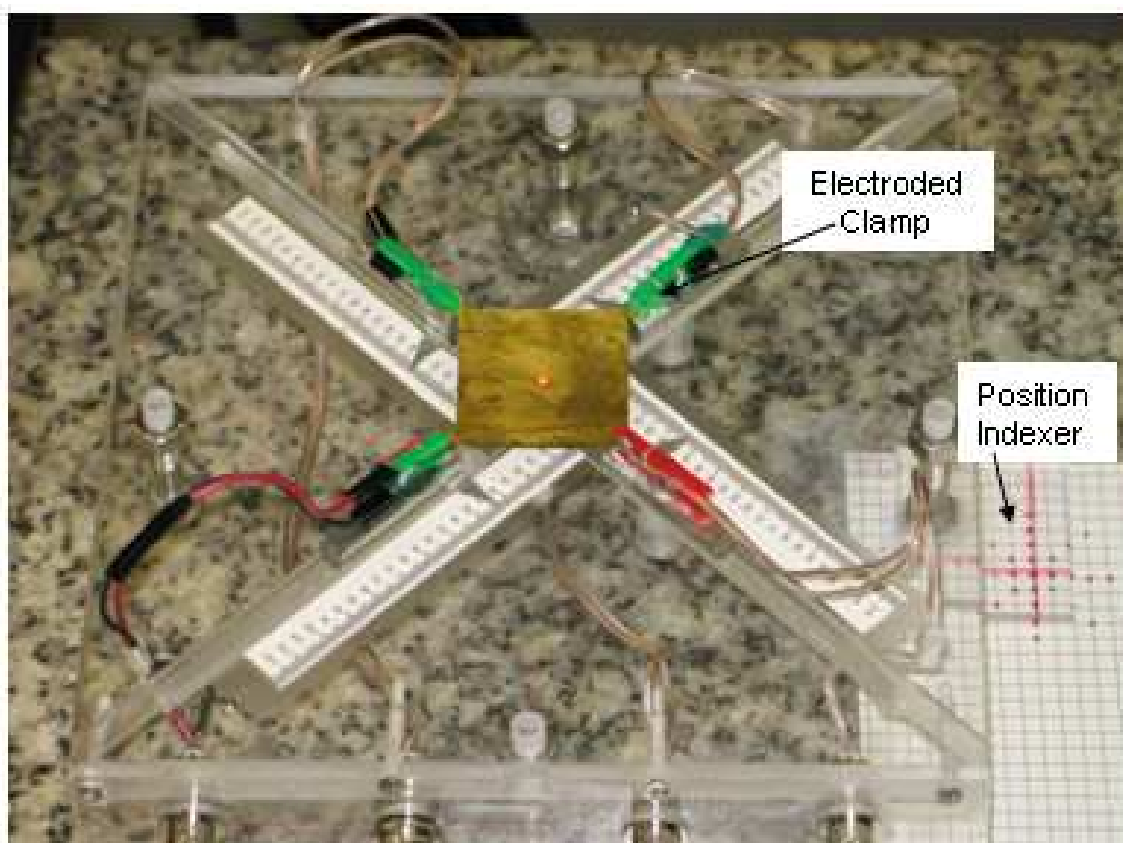


Figure 4.7: Experimental test fixture

The laser vibrometer remained stationary and the fixture was moved to take measurements at many locations to resolve the deflection shapes spatially. A set of cross hairs are attached to the fixture and these cross hairs are placed grid paper so that the measurements can be taken at prescribed locations. The structure is substantially more stiff

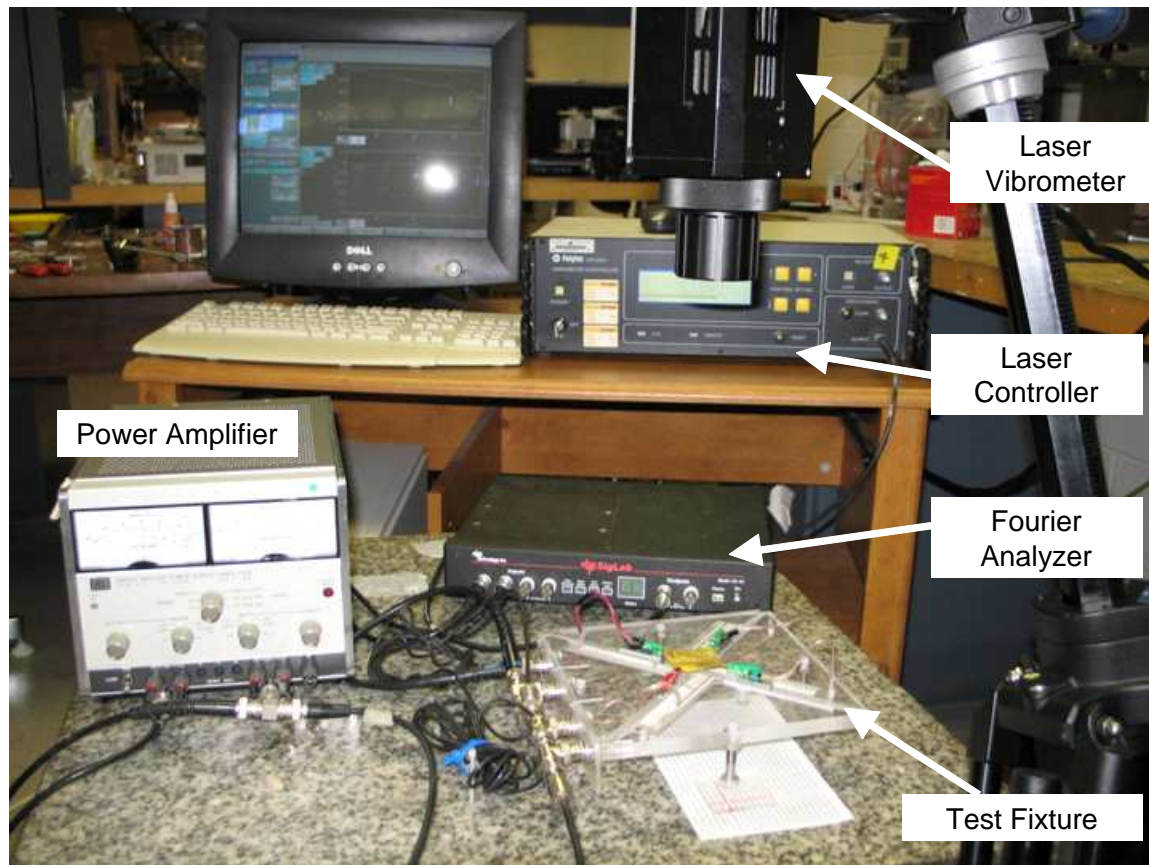


Figure 4.8: Experimental test setup

mechanically than the cantilever beam sample so a larger input voltage was required to get an acceptable signal to noise ratio. The input signal was set to 0.5 V_{rms}, which is about twice the voltage used during the materials characterization experiments. Once acceptably clean signals were achieved we proceeded to measure the frequency response to a random electrical excitation at 41 of the 81 possible points on a 4 mm spaced grid. The Fourier analyzer averaged 50 measurements. Four such measurements are shown in Figure 4.9. The location of these points is indicated at the center as well as the location of all 41 measurements. Because the specimen, loading, and boundary conditions are nearly symmetric we expect to see symmetric operating shapes. This expectation was found to be mostly correct. The measurement at $x = 4$ mm $y = 4$ mm is very similar to the measurement at $x = -4$ mm

$y = 4$ mm. The antiresonance at about 120 Hz does not appear in the measurement at $x = -4$ mm $y = 4$ mm; however at higher frequencies they match fairly well and while the phase plots are different the difference is 360 degrees.

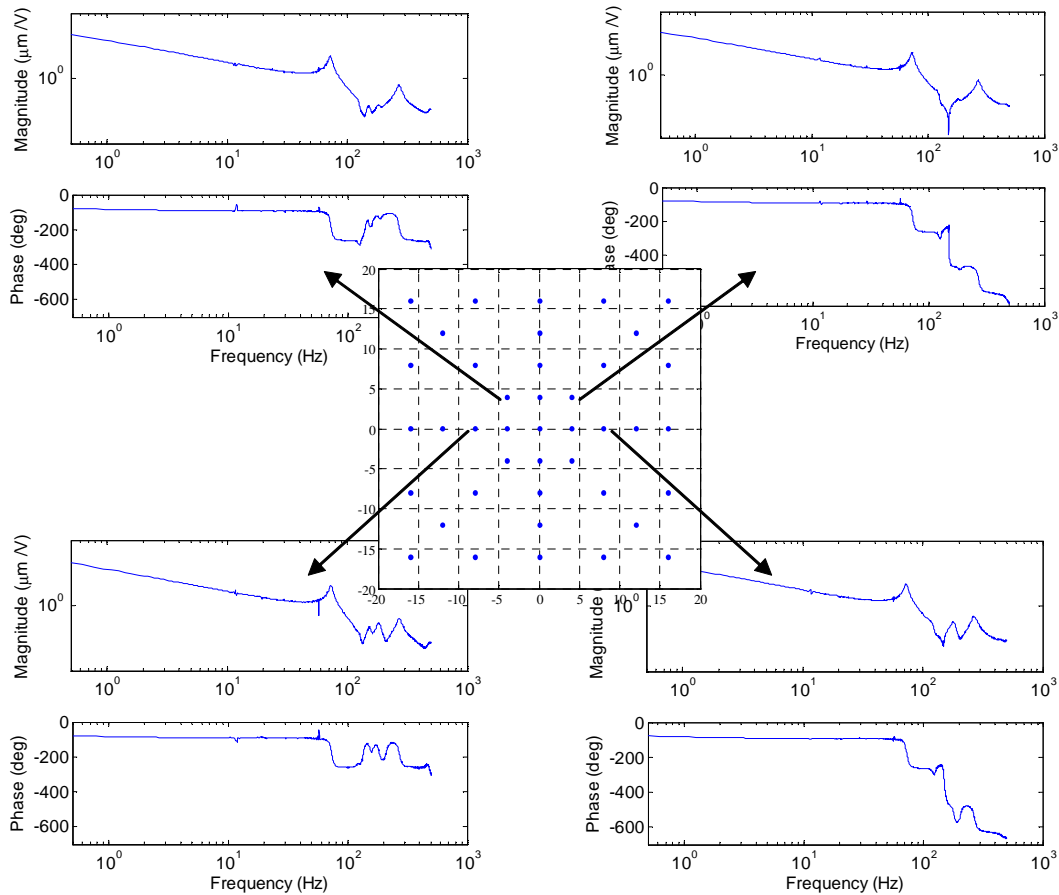


Figure 4.9: Measurement points

4.2.4 Experimental Results and Model Validation

Our initial comparison between the experimental data and a simulation was a frequency response for the center of the plate. The first simulation for a center point response did not compare well with the experimental results. Figure 4.10 shows that the low frequency response was much higher in the simulation and the resonances occurred about 23 Hz while the experiment indicates that the first resonance is at about 70 Hz. From the start it was acknowledged that the corner pinned boundary condition would be difficult to achieve experimentally, so to better match the experimental data torsional springs were modeled

at the corners using the additional potential energy term introduced at the beginning of this chapter. The spring constant were used as a model updating parameter. They were adjusted until the simulations matched the experiment better. However, this method alone proved inadequate because the effect of the torsional spring is limited. Once the spring constant gets high enough the deflection shapes have no slope at the corner points and further increase of the spring constant has no effect. That limit is shown in Figure 4.10 and is labeled Torsional Spring. The first resonance frequency was only increased to about 45 Hz, which is still a large error.

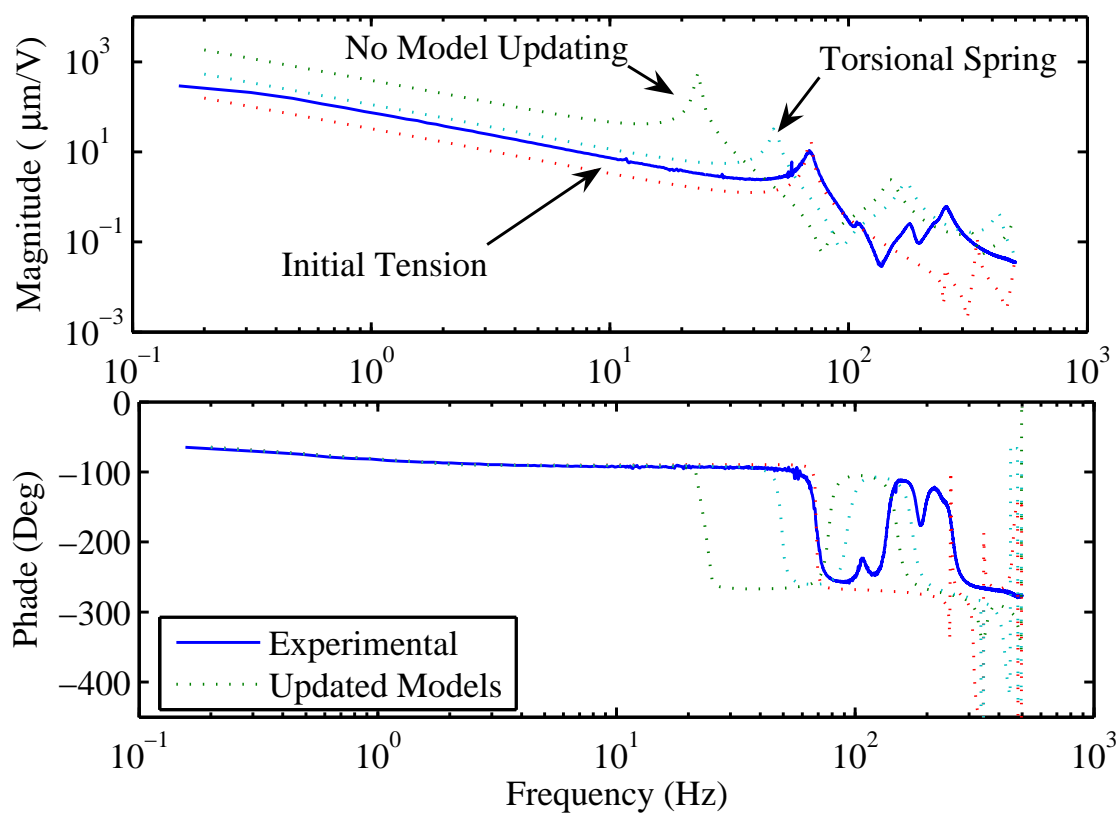


Figure 4.10: Effect of model updating at the center point

Next, we hypothesized that when the polymer was clamped into the test fixture some initial tension was likely induced so we included a uniform initial tension in the model and adjusted that until the first resonance frequencies matched. With an initial tension of 26 N/m we were able to match the first resonance frequency, but the magnitude of the peak was greatly exaggerated. The exaggeration is most likely because with the tension

this high the stiffness is dominated by the tension and the viscoelasticity of the material is insignificant. The shape of the frequency response at higher frequencies is also greatly affected by the initial tension. The frequencies of the next few resonances are much higher in the simulation than the experiments and the magnitudes are much lower.

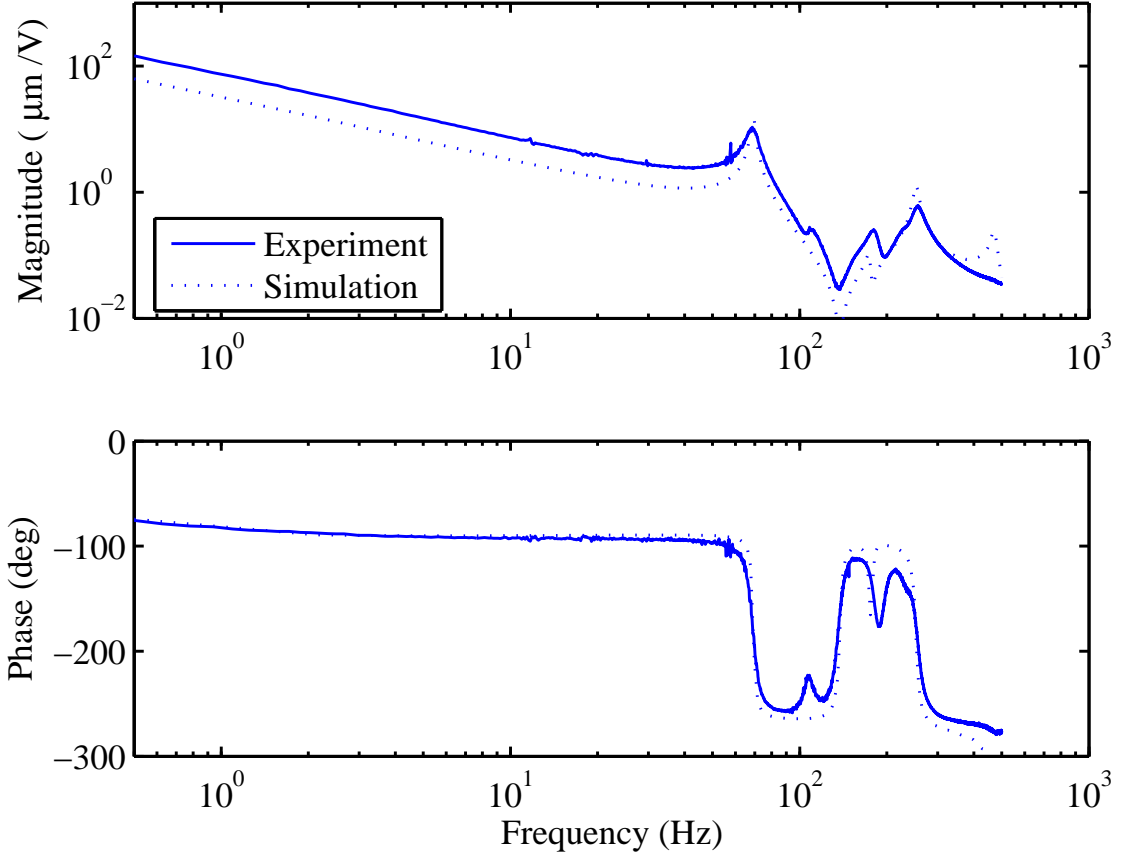


Figure 4.11: Comparison of experiment and simulation at the center point

A much better fit was achieved using a combination of the boundary stiffness and initial tension. The best fit is compared to the experimental data in Figure 4.11. This fit was achieved with an initial tension of 9 N/m and torsional spring constants of 5 mN-m/rad. The model does a good job of predicting the first, third and fourth resonance frequencies and the shape of the curve matches well with the exception of a mode which is close in frequency to the first resonance. This mode is likely because of asymmetries in the boundary conditions or the material. Also the low frequency magnitude of the simulations is lower than the model predicts. It has been shown that the electrical impedance changes with input voltage (Kothera and Leo, 2005). This may account for the discrepancy because

the material parameters were identified at 250 mVrms while the plate experiments were performed at 500 mVrms.

In addition to the center point comparison, Figure 4.12 shows a comparison of experimental data and a simulation at the position $x = 4 \text{ mm}$ $y = 4 \text{ mm}$. Again the simulation slightly under predicts the low frequency magnitude, but the resonances are in good agreement and more importantly the overall shape compares well. The experiment still shows a small resonance at about 108 Hz which does not appear in the model, but beyond that there is good agreement. There appears to be disagreement in the phase plot after the first anti-resonance, but the phase differential is 360 degrees so shapes are not affected. The discrepancy is likely because that anti-resonance is a non-minimum phase zero.

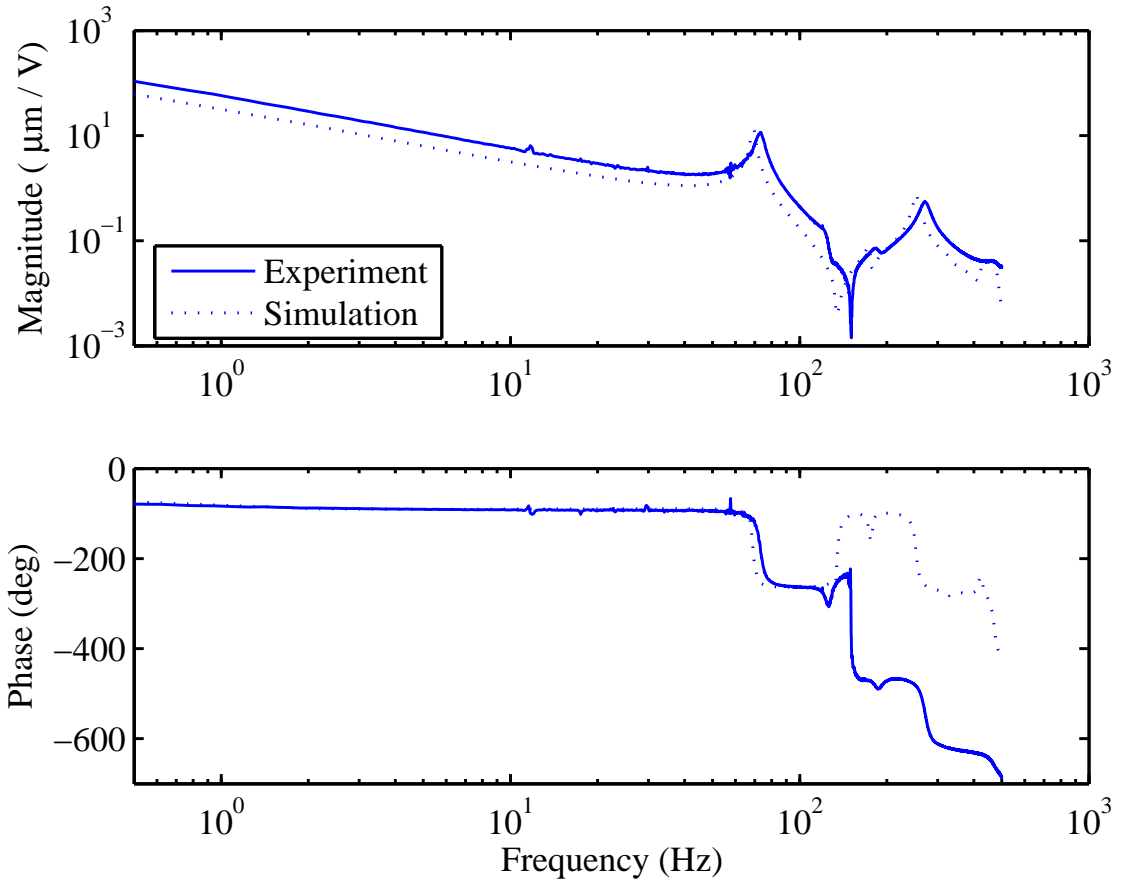


Figure 4.12: Comparison of experiment and simulation at ($x=4\text{mm},y=4\text{mm}$)

The previous frequency response functions were both on lines between two of the boundary conditions, which suggests they are likely lines of symmetry. Referring back to Figure 4.9, the only measurement points not on a horizontal, vertical, or diagonal line are

very near the edges of the plate. A comparison of the experimental data and the simulation at point $x = 16$ mm $y = 8$ mm is shown in figure 4.13. The resonance at about 108 Hz is more pronounced at this point which is consistent with our belief that it was due to an asymmetry in either the boundary conditions or the material. The shape of the third and fourth peaks still compares very well with the experiments, and with the exception of the phase drop due to that second mode the shape of the phase plot is an exceptional match.

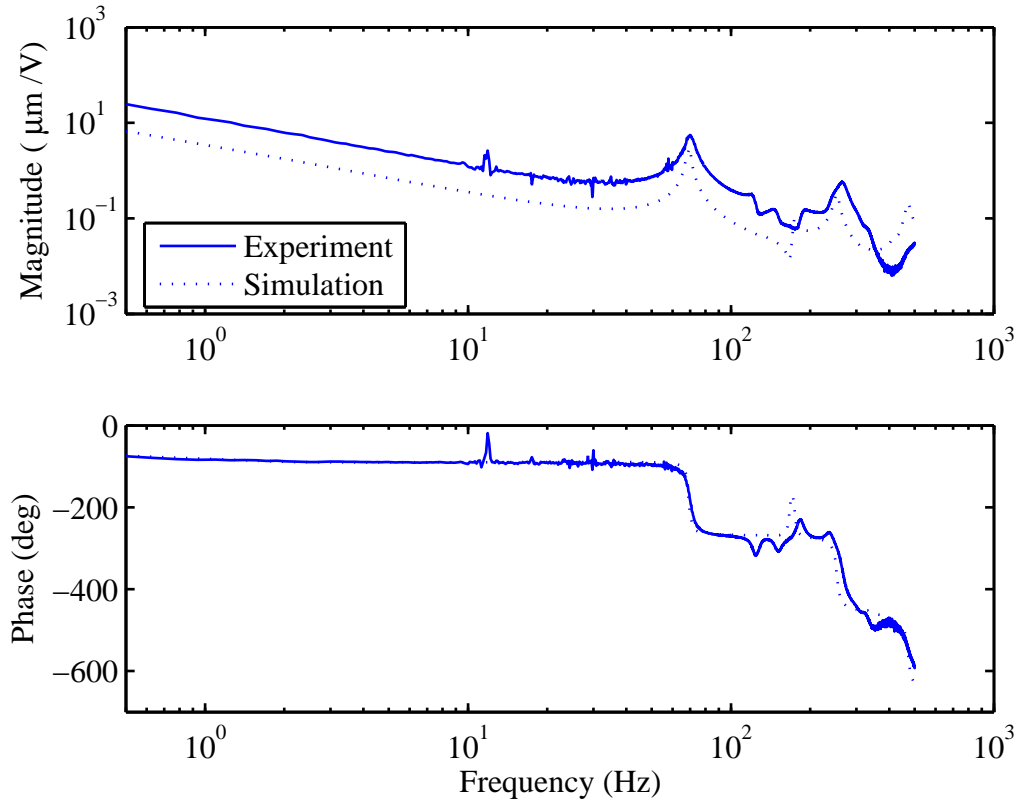


Figure 4.13: Comparison of experiment and simulation at $(x=16\text{mm}, y=12\text{mm})$

Comparisons were also performed between measured deflection shapes and those computed by simulations. The first mode which occurs at about 70 Hz is shown in Figure 4.14. The general trend of the shapes match very well. The maximum simulated displacement is displacement is $13.72 \mu\text{m}$ while the maximum measured displacement was $12.52 \mu\text{m}$. Additionally the maximum displacement in the simulation occurred, as expected for the first mode, at the center point while the experimental data shows the maximum to be at $x = 4$ mm $y = 0$ mm. This is due to the noticeable dip in the region near the center of the experimental results. This could also be because of assymmetric boundary conditions;

however, we attempted to reproduce this result by applying different spring constants at each corner, but were unsuccessful. The more likely cause by the non-uniformity in the material. It could be a localized mass or stiffness. The displacement at the edges of the simulation is also a slightly more than the displacement near the edge in the test specimen; however, they are close and it is encouraging that in both the experiment and the simulation the displacement along the long edge is higher than the displacement along the short edge.

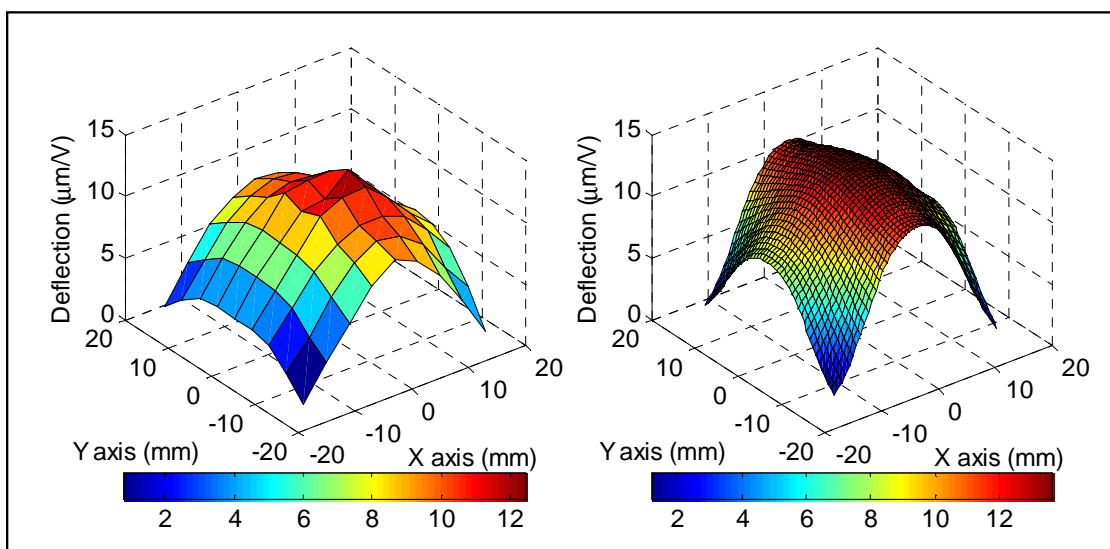


Figure 4.14: Comparison of simulated and experimental deflection at 70 Hz

The next shape comparison was at 108 Hz which is the frequency of the second resonance that appeared in the experiment, but did not show up in the model. An ideal square plate has repeated modes at each frequency due to symmetry. Because of this it was assumed that the second mode would be similar to the first mode, but the experimental results, which are shown in Figure 4.15 indicate a completely different shape. In fact the shape is very similar to the shape seen at the third resonance. Though there was no peak in the simulated transfer functions we looked at the simulated shape at that frequency. The general shape was similar to the experiment though it was more symmetric. The magnitudes were also much less than the experiment, but that is expected since a peak did not appear in the transfer function. The shapes were both very similar to the shapes which occurred at the third resonance. Figure 4.16 shows a comparison of the simulation and experiment at 180 Hz. The experimental shape looks very much like the second shape only rotated 45 degrees about the z axis. This explains why the second shape did not resemble the first

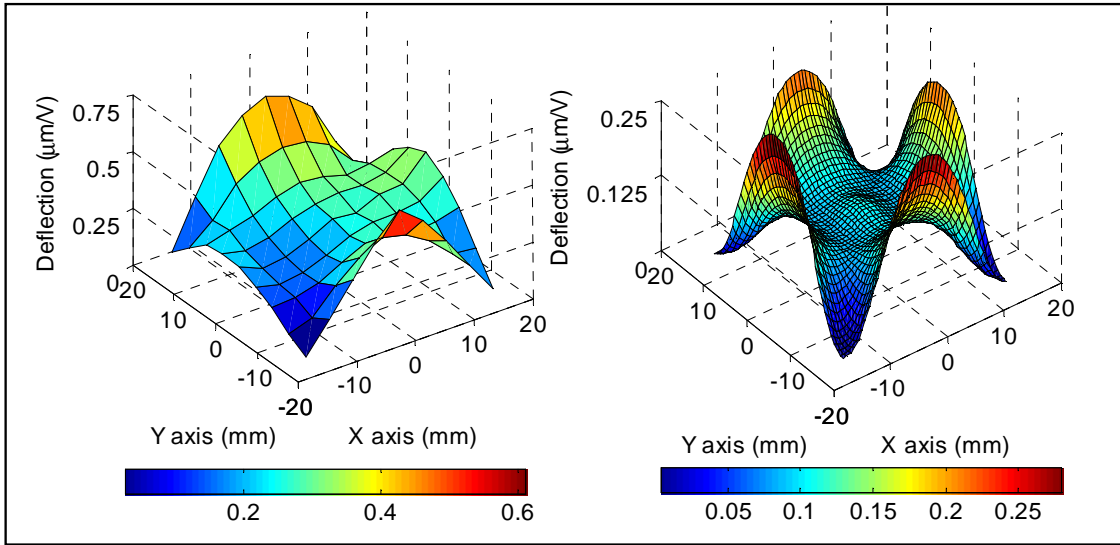


Figure 4.15: Comparison of simulated and experimental deflection at 108 Hz
shape.

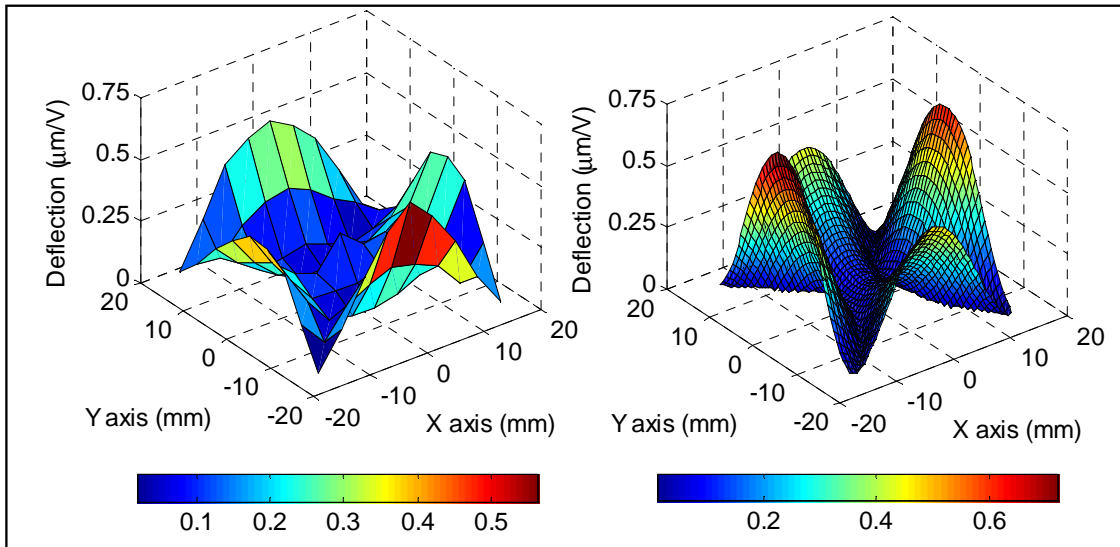


Figure 4.16: Comparison of simulated and experimental deflection at 180 Hz

The fourth deflection shapes are compared in Figure 4.17. The magnitude of the center section is a little larger than the simulation, but the overall shape matches very well. The discrepancy in the center is common to all the shapes and indicates that there is some local phenomenon such as mass or stiffness that has not been included in the model. This will not be a great problem as manufacturing methods are improved resulting in more

uniform materials.

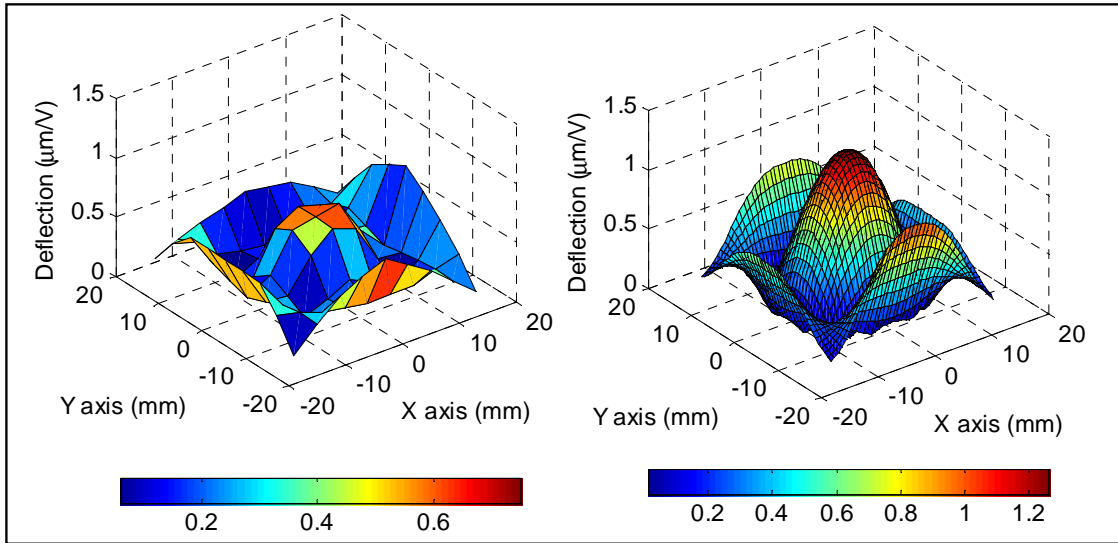


Figure 4.17: Comparison of simulated and experimental deflection at 265 Hz

4.3 Chapter Summary

In this chapter we first demonstrated a plate model developed in cylindrical coordinates and some of the predictions that can be obtained from the simulations. Then we expanded the potential energy function originally discussed in Chapter 2 and applied this expanded potential energy function to a plate model in cartesian coordinates. The potential energy due to pre-stress that is uniform through the thickness can be modeled like the potential energy of a pre-tensioned membrane. Non-homogeneous boundary conditions were handled in this model by including torsional springs in the system. These techniques were applied to model a non-ideal system. The resulting simulations matched the experimental results very well and showed that the variational method developed in this work is valid for plate type structures.

Chapter 5

Conclusions

This thesis has demonstrated a variational approach to modeling structures containing ionomeric components. The three primary research goals were accomplished and are reiterated below with some additional discussion.

5.1 Accomplishments and Contributions

- *Development of a variational modeling method for multiple system configurations.* In Chapter 2 we demonstrated the variational method as it applied to an as yet undefined structure. Energy functions were defined by operations which are applied to shape functions associated with the structure and boundary conditions. The energy functions were then substituted into Hamilton's Principle resulting in a set of second order differential equations which were written in matrix form and transformed into the frequency domain. Solution of the differential equation resulted methods for computing the deformation and charge response as a function of applied voltage or force. This method is applicable to any system. The difficulty with applying the method to very complex structures will be in defining a set of shape functions which satisfy the geometric boundary conditions.
- *Develop reciprocal modeling methods.* The method demonstrated in Chapter 2 results in a frequency domain matrix equation which when solved results in general coordinates related to both mechanical and electrical displacements. Therefore, the model as developed is capable of taking either mechanical or electrical inputs and return-

ing either mechanical or electrical outputs. This allows a design engineer to use the model to assist in designing either actuation or sensing systems based on ionomeric materials.

- *Refinement of methods to characterize the material properties.* Though the formulation took a slightly different direction the main difference between this work and that performed by Hagood is the materials we have investigated. Hagood applied the variational method to structures containing piezoelectric components, which at low to medium frequencies exhibit little to no frequency dependence. More importantly piezoelectric are purely dielectric materials unlike ionic polymers which exhibit resistive as well as capacitive properties. Because of the strong frequency dependence in the material it is important to have a good estimation of material properties as inputs to the modeling method. Previous work by Newbury, Franklin, and Leo demonstrated methods for determining these properties. Newbury demonstrated that his methods were valid for frequencies below the first resonance of a cantilever beam (Newbury and Leo, 2003a). Franklin then extended Newbury's method for determining the elastic modulus to higher frequencies but continued to apply some assumptions that were valid only at low frequencies to determine the permittivity and strain coefficients. Here we have reiterated Franklin's method of determining the viscoelastic parameters which define the modulus. Then we determined the permittivity without making any low frequency assumptions. Finally, we showed how a cantilever beam model can be used to determine the strain coefficient. This method of determining the strain coefficient also does not make any low frequency assumptions; however, it requires good estimation of both the elastic modulus and permittivity in order to achieve an accurate estimation of the strain coefficient parameters.

In addition to achieving these three main goals related to modeling methods this thesis presented an extensive model validation study. In Chapter 3 we showed an excellent agreement between measured and simulated frequency response functions up to 500 Hz. We also showed very good agreement between simulated deflection shapes and shapes that were measured experimentally. These shapes also corresponded very well with the shape functions that were chosen. A very important result presented in Chapter 3 is the correlation between simulated and experimental sensing response functions. This result validates the

energy approach as the modeling method and shows that the potential energy function we have used can be applied to materials which are not entirely dielectric. Chapter 4 showed a validation very similar to the validation of Chapter 3. We were only concerned with mechanical response in the chapter so the validation did not include any sensing results, but the frequency responses and deflection shapes were in very good agreement with the exception of some asymmetries that will become less dominant as the size of the structure is increased.

It has been shown that good estimates of the material properties are essential. In Chapter 3 we attributed some small error in the damping estimates of the model to inaccuracies in the viscoelastic parameter identification. The resulting errors were acceptable; however, further refinement of the model may require less uncertainty in the parameter estimation.

The method was demonstrated on three representative structures. First we developed a cantilever beam model, which was initially applied to materials characterization, but is potentially an excellent sensor configuration. Next, we developed a plate model in cylindrical coordinates. We applied exactly the same methodology to the structure in two dimensions as we applied to the beam model. The shape functions and differential operators which related strain to displacement were different but the method remained the same. Different boundary conditions can be applied using two methods. First, any homogeneous boundary conditions should be reflected in the shape functions; however, in the case of the square plate we demonstrated the application of a non homogeneous boundary condition. This was applied by choosing shape functions which would not violate the boundary conditions and then modified the potential energy function to include the outside influence of the non homogeneous boundary condition.

5.2 Recommendations for further improvement of this work

The work presented here is fairly complete; however, there are several areas of research which may improve upon the results presented here. These research suggestions are as follows:

- *Improve viscoelastic parameter identification.* In this work the frequency dependent elastic modulus was identified from stiffness measurements of a sliding pinned beam.

The results were actually very good; however, measurements performed in pure tension may be advisable for two reasons. First, the mass properties of the beam dominate the response at higher frequencies in bending so inaccuracies in the modulus may be overshadowed by the beam dynamics in the curve fit. Second, while the testing method developed by Franklin was an improvement on the cantilever beam configuration developed by Newbury the form of the stiffness transfer function does not allow the separation of the modulus from the beam dynamics. Ideally we would have a transfer function of the form

$$K(\omega) = Y(\omega)C_2(\omega) \quad (5.1)$$

where $K(\omega)$ is the measured stiffness $Y(\omega)$ is still the frequency dependent modulus, and $C_2(\omega)$ represents the dynamics of the test specimen. In this way we could separate the elastic modulus from the dynamics and get a better idea of what the form of the transfer function should be just as we did when determining the permittivity.

- *Investigate methods for transforming the solution back into the time domain.* Methods exist which involve separating the loss terms from the GHM parameters in the modulus and writing them as additional degrees of freedom in the mass and stiffness matrices (McTavish and Hughes, 1993). The application of these methods to the permittivity and strain coefficient parameters would allow a time domain representation of the equations. Resonant frequencies and damping could then be determined using eigenvalue methods such as are commonly employed in vibration problems (Inman, 2001). Additionally, a time domain representation would allow implementation of optimal control methods.
- *Perform validation experiments on structures which include passive materials.* While this method is easily applicable to structures with passive components this study did not include any validation of models which includes passive components. It is possible though unlikely that some unforeseen coupling could occur between the ionomeric components and the passive components. A set of successful validation experiments would help convince the engineering community that this modeling method fits their needs.
- *Investigate the behavior of multiple input system.* In this study experiments only

involved a single electrical input. It is possible that in a multiple electrical input system there could be some coupling between electrodes which would require a more complex electrical shape function. A study could be performed to determine the if this coupling is present and if it has a significant impact on the accuracy of the simulations.

Bibliography

- Akle, B. J., Bennett, M. D., and Leo, D. J., *High-Strain Ionomeric-Ionic Liquid Composites Via Electrode Tailoring*, **Proceedings of IMECE 2004**, , No. 61246, 2004.
- Bennett, M. and Leo, D., *Ionic liquids as stable solvents for ionic polymer transducers*, **Sensors and Actuators**, Vol. A, No. 115, pp. 79–90, 2004.
- Blevins, R. D., **Formulas for Natural Frequency and Mode Shape**, Krieger Publishing Company, Malabar, Florida, 1995.
- Chang, K. H. and Hagood, N. W., *Modeling of nonlinear piezoceramics for structural actuation*, **SPIE Proceedings**, Vol. 2190, pp. 194–205, 1994.
- Franklin, J. W., 2003, **Electromechanical Model of Encapsulated Ionic Polymer Transducers**, M.S. Thesis, Virginia Polytechnic Institute and State University.
- Gere, J. M. and Timoshenko, S. P., **Mechanics of Materials**, Fourth Edition, PWS Publishing Company, Boston, MA, 1997.
- Inman, D., **Engineering Vibrations**, Second Edition, Prentice-Hall, Upper Saddle River, NJ, 2001.
- Kanno, R., Kurata, A., Hattori, M., Tadokoro, S., Takamori, T., and Oguro, K., *Characteristics and Modeling of ICPF Actuator*, **Proc. Japan-USA Symposium on Flexible Automation**, pp. 691–698, 1994.
- Kothera, C. and Leo, D., *Characterization of the solvent-induced nonlinear response of ionic polymer actuators*, **Proceedings of SPIE**, Vol. 5757-37, No. 4, 2005.
- McTavish, D. and Hughes, P., *Modeling of Linear Viscoelastic Space Structures*, **Journal of Vibration and Acoustics**, Vol. 115, pp. 102–110, 1993.

Meirovitch, L., **Principles and Techniques of Vibrations**, Prentice-Hall, Upper Saddle River, NJ, 1997.

Nemat-Nasser, S. and Li, J. Y., *Electromechanical response of ionic polymer-metal composites*, **Journal of App. Physics**, Vol. 87, No. 1, pp. 3321–3331, 2000.

Nemat-Nasser, S. and Thomas, C. W., 2001, “Topic 6 Ionomeric Polymer-Metal Composites,” in: **Electroactive Polymer (EAP) Actuators as Artificial Muscles**, ed. Y. Bar-Cohen, SPIE press, pp. 140–191.

Newbury, K. M. and Leo, D. J., *Electromechanical Modeling and Characterization of Ionic Polymer Benders*, **Journal of Intelligent Material Systems and Structures**, Vol. 13, pp. 51–60, 2002.

Newbury, K. M. and Leo, D. J., *Linear Electromechanical Model of Ionic Polymer Transducers Part I: Model Development*, **Journal of Intelligent Material Systems and Structures**, Vol. 14, No. 6, pp. 333–342, 2003a.

Newbury, K. M. and Leo, D. J., *Linear Electromechanical Model of Ionic Polymer Transducers Part II: Experimental Validation (Revised)*, **Journal of Intelligent Material Systems and Structures**, Vol. 14, No. 6, pp. 343–357, 2003b.

Reed, R., *Comparison of Methods in Calculating Frequencies of Corner-Supported Rectangular Plates*, **NASA**, Vol. TN D-3030, 1965.

Tadokoro, S., Takamori, T., and Oguro, K., 2001, “Chapter 13 Modeling IPMC for Design of Actuation Mechanisms,” in: **Electroactive Polymer (EAP) Actuators as Artificial Muscles**, ed. Y. Bar-Cohen, SPIE press, pp. 331–366.

Tadokoro, S., Yamagami, S., Takamori, T., and Oguro, K., *Modeling of Nafion-Pt composite actuators (ICPF) by ionic motion*, **SPIE Proceedings**, Vol. 3987, pp. 92–102, 2000.

Vita

Miles Buechler was born to Jerry and Mary Buechler in Elko, NV, but moved to Billings, MT at a very young age. He lived and played in different parts of Montana until 1988 when he returned to Elko. He completed high school in Elko where he concentrated his studies on vocational courses such as *Automotive Repair* and *Welding*. After graduation he joined the United States Marine Corps where he served as a Rifleman, Marksmanship Instructor, and Helicopter Mechanic. His duties as a mechanic lead him to work closely with engineers who were responsible for giving technical assistance to aircraft maintenance personnel. These engineers convinced him that he could do more for his country as an Engineer than as a mechanic so at the end of his enlistment he accepted his Honorable Discharge and returned to civilian life. Having saved little money while serving in the Marine Corps, he worked as mechanic at a gold mine near Elko for one year before beginning his academic career at Montana State University. The summer preceding his senior year he was accepted into the Los Alamos Dynamics Summer School which is organized by Dr. Charles Farrar. During this program he was introduced to modal analysis and smart materials. He then received his Bachelors in Mechanical Engineering in May 2003, and accepted a teaching assistantship at Virginia Tech where he hoped to be able to work with smart materials in the Center for Intelligent Materials Systems and Structures. During his first semester as a masters student he attended a *Smart Materials* course taught by Dr. Donald Leo. In addition to learning techniques which would soon become valuable to his masters research he developed a working relationship with Dr. Leo. Following the course Dr. Leo offered Miles a project involving modeling structures based on ionic polymers. This project stimulated miles to learn things he never would have simply in a classroom environment. Upon completion of his degree he will return to Los Alamos National Laboratory where he will work in a simulations and analysis group.